High-order symmetrical hyperbolic wavelets

Khoa N. Le*

Gold Coast campus, Griffith School of Engineering, Griffith University, Parklands Drive, Southport QLD4215, Australia

Received 28 March 2006; accepted 3 March 2007

Abstract

This paper studies high-order wavelets of the first-order hyperbolic, Choi–Williams (CW) and nth-order hyperbolic kernels for analyses of digital time series, by using their second- and higher-order derivatives. For time-domain investigations, normalisation constants of the second-, fourth-, sixth-, eighth- and tenth-order hyperbolic and CW wavelets are numerically given. For frequency-domain investigations, wavelet parameters including band-peak frequencies, minimum numbers of sampling points, scale limits, scale resolutions and total number of scales are explicitly given and numerically estimated for the fourth-order hyperbolic and CW wavelets. Parameter comparisons among the Morlet wavelet, hyperbolic and CW second- and fourth-order wavelets are also given. Detection of periodicity and chaos in the Duffing oscillator is discussed.

1. Introduction

1.1. Motivation

Time–frequency signal processing has been one of the main areas in signal processing for many years. Cohen's generalised time–frequency distribution has been well known and found many applications [1,2]. The most useful feature of Cohen's time–frequency distribution is the involvement of a kernel function $\Phi(\theta,\tau)$ which uniquely determines properties of its time–frequency distribution. A number of kernels have been proposed over a time period of nearly 50 years in which the unity kernel, Wigner–Ville $\Phi(\theta, \tau) = 1$, is the simplest. In 1989, Choi–Williams (CW) kernel [3] was proposed and shown to be more effective in cross-term suppression than Wigner–Ville kernel. In 1995, Costa and Boudreaux-Bartels [4] proposed a multiform tiltable exponential kernel which further improves cross-term suppression and auto-term support. However, various types of this kernel cannot be explicitly derived. The first-order hyperbolic kernel $\Phi(\theta,\tau) = [\mathrm{sech}(\beta\theta\tau)]^{n\,=\,1}$ and hyperbolic kernel family [5] were proposed and have been shown to be more effective than CW kernel in terms of cross-term suppression and noise robustness. A complete survey of all kernels for Cohen's generalised time–frequency distribution is given in Refs. [1,2,5].

*Tel.: +61 0423 035 916; fax: +61 07 5552 8065.

E-mail address: K.Le@griffith.edu.au.

To be an admissible kernel, $\Phi(\theta,\tau)$ must satisfy seven constraints that were extensively investigated in Refs. [1,2,5–8]. Typical examples on kernel-wavelet relations were shown in Ref. [9] for the first-order hyperbolic and CW kernels on one hand, and for the hyperbolic and Mexican-hat (CW) wavelets on the other hand, in which the kernels' negative second-order derivatives were employed to obtain the two wavelets. Because of its locality and positivity in the frequency domain, the second-order kernel derivative, called Laplacian operator $\nabla^2 = \partial^2/\partial x^2 + \partial^2/\partial y^2$ [10,11], has been used to detect image zero-crossings and intensity changes. It was also shown by Marr that the operator can be tuned to detect fine changes such as edge detection in images, moreover, it is a differential operator which allows explicit calculations of higher-order derivative functions. The works reported in Refs. [5,9] have motivated further studies on higher-order derivatives (higher-order Laplacian operators) of the first-order hyperbolic, CW and nth-order hyperbolic kernels. This might also lead to discoveries of new kernels and wavelets, and consequently, opens up new research directions on wavelets and their useful applications. It should also be stressed that currently there are two symmetrical wavelets that have been widely employed, namely Morlet and Mexican-hat wavelets. Thus proposals of new symmetrical wavelets play an important role in possibly improving previous results obtained by using the Morlet and CW wavelets.

According to Addison et al. [12], symmetrical wavelets including Morlet and CW which may be considered as second-order wavelets generated from their corresponding kernels, have often been overlooked in the literature even though they have found many applications in various disciplines, in particular detection of coherent structures in turbulence and in ECG signals [13]. Thus it is believed that there are still new ideas and further improvements in using higher-order symmetrical wavelets. The aims of this paper are as follows. Firstly, to show that high-order derivatives of admissible kernels used in Cohen's time–frequency distributions are admissible wavelets. Secondly, high-order hyperbolic and CW wavelet parameters including band-peak frequencies, minimum numbers of sampling points, scale limits, scale resolutions and total number of scales are numerically estimated and rigorously compared using typical values of wavelet parameters β and σ.

This paper extends the work carried out in [9,14] and reports new results on high-order symmetrical hyperbolic wavelets, which can be used to analyse digital time series. The paper is primarily devoted to investigate in detail these wavelets' mathematical properties by explicitly deriving and numerically estimating their useful parameters as outlined in detail in Ref. [14]. In view, this paper can be considered as the foundation for further work on higher-order hyperbolic wavelets in one hand and on other higher-order symmetrical wavelets such as Morlet wavelet in the other hand. In addition, the paper is also devoted to explain the origin of these wavelets and their close relations to kernels used in Cohen's time–frequency distributions.

1.2. Paper structure

The paper can be divided into two parts. The first part discusses time-domain properties of the hyperbolic and CW high-order wavelets by checking their zero-mean admissibility constraints, calculating normalisation constants and presenting graphical plots. The second part explicitly calculates and numerically estimates the hyperbolic and CW wavelet parameters including band-peak frequency, minimum number of sampling points, scale limits, scale resolution, maximum number of scales and total number of scales. The Duffing oscillator is used as a case study to show the effectiveness of hyperbolic and CW high-order wavelets. There are three different high-order wavelet types which are generated from three kernels: first-order hyperbolic, CW and nth-order hyperbolic, in which the first two will be extensively studied. The last wavelet type is explicitly given in terms of the kernel order n and not numerically estimated.

The paper is organised as follows. An important relation among kernels and wavelets is discussed via the meaning of kernels' even-order derivation (Section 2) and positive concavity (Section 3), from that, admissible wavelets can be identified. Hyperbolic and CW wavelet normalisation constants are numerically estimated for $\beta = 1$ and $\sigma = 2$. Sections 4 and 5 explicitly derive high-order hyperbolic and CW wavelet frequency parameters which are also numerically estimated in Section 6. Section 7 studies Duffing oscillator using high-order hyperbolic and CW wavelet transforms and wavelet power spectra. Section 8 concludes main ideas that have been discussed in the paper and briefly outlines future work.

2. Relationship between time–frequency kernels and wavelets

The second-order derivatives of the first-order hyperbolic and CW kernels are symmetrical and satisfy an admissibility constraint of having zero areas under their graphs as explained in Ref. [9]. The zero-mean admissibility constraint, which is the wavelet's area under its graph, must be zero and is given by [1,2,9,15,16]

$$\int_{-\infty}^{+\infty} \psi(t)\,\mathrm{d}t = 0, \tag{1}$$

where $\psi(t)$ is the wavelet function.

It is important to stress that not all functions that satisfy the admissibility constraint given by Eq. (1) are admissible wavelets. Moreover, to be an admissible wavelet, a function must have finite energy, i.e. finite time support. The simplest wavelet, Haar, comprises of two rectangular square waves of finite time support [15,16] from 0 to 1. The periodic sinusoidal function, which has been used in Fourier series expansions and Fourier transforms, even though meets the admissibility constraint, cannot be considered as an admissible wavelet because of its infinite energy and time support. For completeness, the continuous wavelet transform of a function $x(t)$ is given by

$$WT(a,b) = \int_{-\infty}^{+\infty} x(t)\psi\left(\frac{t-b}{a}\right)\mathrm{d}t, \tag{2}$$

where $\psi((t-b)/a)$ is the wavelet function.

The Mexican-hat (Choi–Williams) wavelet and second-order hyperbolic wavelet [9,13] were generated by taking negative second-order derivatives [15] of the CW and first-order hyperbolic kernels, respectively. To be an admissible kernel, a function must meet kernel admissibility constraints which are given as [1,2,5–8]

1. Kernel function, $\Phi(\theta,\tau)$, is independent of time t,
2. Kernel function is independent of frequency ω,
3. $\Phi(\theta,0) = 1$ for all θ,
4. $\Phi(0,\tau) = 1$ for all τ,
5. Kernel function must be real, i.e. $\Phi(\theta,\tau) = \Phi^*(-\theta,-\tau)$, where "*" indicates the complex conjugate,
6. $\left.\dfrac{\mathrm{d}}{\mathrm{d}\tau}\Phi(\theta,\tau)\right|_{\tau=0} = 0, \quad \forall \theta,$
7. $\left.\dfrac{\mathrm{d}}{\mathrm{d}\theta}\Phi(\theta,\tau)\right|_{\theta=0} = 0, \quad \forall \tau.$

To obtain admissible wavelets, there are two main issues that need to be considered

- Why have second- and even higher-order kernel derivatives been used? It should be noted that the first- and odd higher-order derivatives have not been considered;
- Why has "negativity" been employed?

To answer the first question, consider the Fourier series expansions of a function $f(x)$ which are given by Eqs. (3) and (4), respectively [17]

$$f_{\mathrm{odd}}(x) = \sum_{n=1}^{+\infty} b_n \sin\left(\frac{n\pi}{L}x\right), \tag{3}$$

where b_n's are Fourier expansion coefficients, and

$$f_{\mathrm{even}}(x) = a_0 + \sum_{n=1}^{+\infty} a_n \cos\left(\frac{n\pi}{L}x\right), \tag{4}$$

where L is the half period of $f(x)$, a_0 and a_n's expansion coefficients.

From Eq. (3), it is clear that when $f(x)$ is odd, it is approximately represented by a sum of odd sinusoidal functions, which have infinite energy, and therefore is not an admissible wavelet function. Thus, admissible wavelet functions must not be odd functions which means that odd-order derivatives are not admissible wavelets and will not be discussed in this paper. The answer to the second question will be given in the next section.

3. Time-domain investigations of hyperbolic and CW high-order wavelets

In this section, normalisation constants of the hyperbolic and CW wavelets with orders 2–10 numerically estimated for $\beta = 1$ and $\sigma = 2$. Wavelets with orders 2–10 generated from the nth-order hyperbolic kernel are explicitly expressed, but their explicit normalisation constants are not given due to extensive mathematics which is beyond the scope of this paper. For all graphs in this section, the typical value of $\beta = \sigma = 1$ is employed for the hyperbolic and CW wavelets, and normalisation is not included since it is intended to show the true wavelet peaks at the origin. The nth-order hyperbolic, first-order hyperbolic and CW kernels are given by

$$\Phi_{\text{Hy\_}g}(t) = [\text{sech}\,(\beta t)]^n, \tag{5}$$

where $n = 1$ corresponds to the first-order hyperbolic kernel, and

$$\Phi_{\text{CW}}(t) = \exp(-t^2/\sigma), \tag{6}$$

where β and σ are the hyperbolic and CW kernel control parameters, respectively.

The second-order derivatives of the first-order hyperbolic and CW kernels are explicitly given by Eqs. (7) and (8), and graphically plotted in Fig. 1

$$W_{H2}(t) = \frac{-1}{N_{\text{Hyp1\_2}}^{\beta}} \beta^2 \big(\text{sech}\,(\beta t)[\tanh\,(\beta t)]^2 - \text{sech}\,(\beta t)\big(1 - [\tanh\,(\beta t)]^2\big)\big), \tag{7}$$

$$W_{\text{CW2}}(t) = \frac{-1}{N_{\text{CW2}}^{\sigma}} \frac{2e^{-t^2/\sigma}(-\sigma + 2t^2)}{\sigma^2}, \tag{8}$$

where $N_{\text{Hyp1\_2}}^{\beta}$ and N_{CW2}^{σ} are normalisation constants of the second-order hyperbolic and CW wavelets, respectively.
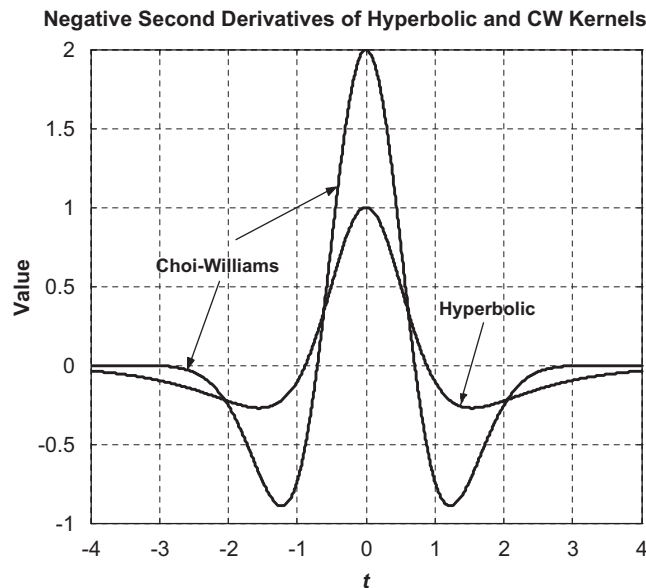

Fig. 1. Negative second derivatives of the first-order hyperbolic and CW kernels for $\beta = \sigma = 1$.

To be an admissible wavelet, a function must satisfy the admissibility constraint given by Eq. (1) of having a zero area under its graph or zero mean [9]. For the second-derivatives of the first-order hyperbolic and CW kernels, their admissibility constraints are explicitly given as follows:

$$C_{H2\_Contraint} = \int_{-\infty}^{+\infty} \frac{-1}{N_{Hyp1\_2}^{\beta}} \beta^2 \left(\text{sech}\,(\beta t)[\tanh\,(\beta t)]^2 - \text{sech}\,(\beta t)\left(1 - [\tanh\,(\beta t)]^2\right) \right) dt = 0, \tag{9}$$

and

$$C_{CW2\_Constraint} = \int_{-\infty}^{+\infty} \frac{-1}{N_{CW2}^{\sigma}} \frac{2e^{-t^2/\sigma}(-\sigma + 2t^2)}{\sigma^2} \, dt = 0, \tag{10}$$

which show that these derivatives are admissible wavelets.

The square normalisation constant of a wavelet $\psi(t)$, which is proportional to its total energy, is calculated by using the following formula [15]

$$\left(N_{wavelet\_name}^{(control\_parameter)} \right)^2 = \int_{-\infty}^{+\infty} [\psi(t)]^2 \, dt = 2 \int_{0}^{+\infty} [\psi(t)]^2 \, dt. \tag{11}$$

It should be noted that normalisation constants are employed so that wavelets have unity peaks at the origin. For the Mexican-hat wavelet, the control parameter value of $\sigma = 2$ is used which approximately yields its normalisation constant of $N_{CW2}^{(\sigma=2)} = \pi^{1/4}\sqrt{3}/2 \approx 1.153$. For other values of σ, the CW normalisation constant N_{CW2}^{σ} is given as

$$(N_{CW2}^{\sigma})^2 = \frac{3}{\sigma} \sqrt{\frac{\pi}{2\sigma}}. \tag{12}$$

Similarly, for $\beta = 1$, the second-order hyperbolic wavelet normalisation constant is given by $N_{Hyp1\_2}^{\beta=1} = \sqrt{14/15} \approx 0.97$. For other values of β, the second-order hyperbolic wavelet normalisation constant $N_{Hyp1\_2}^{\beta}$ is given as

$$(N_{Hyp1\_2}^{\beta})^2 = \frac{14\beta^3}{15}. \tag{13}$$

The third-order derivatives of the CW and first-order hyperbolic kernels are given as

$$W_{H3}(t) = -\frac{\beta^3 \sinh\,(\beta t)\left([\cosh\,(\beta t)]^2 - 6\right)}{[\cosh\,(\beta t)]^4}, \tag{14}$$

$$W_{CW3}(t) = \frac{4te^{-t^2/\sigma}}{\sigma^2} \left(3 - \frac{2t^2}{\sigma} \right). \tag{15}$$

For $\sigma = \beta = 1$, graphical representations of Eqs. (14) and (15) are given in Fig. 2. As can be seen, both third-order derivative functions have zero peaks at the origin, i.e. $f(x) = -f(-x)$, which clearly are odd functions. Since it is necessary that a wavelet possesses a non-zero peak at the origin so that it is "continuous" at $t = 0$, these derivative functions are not useful as explained earlier in Section 2. Mathematically, the fourth-, sixth-, eighth- and tenth-order derivatives of the hyperbolic and CW kernels are given by Eqs. (16)–(23), respectively

$$W_{H4}(t) = \beta^4 \text{sech}\,(\beta t)\{-20[\text{sech}\,(\beta t)]^2 + 24[\text{sech}\,(\beta t)]^4\}, \tag{16}$$

$$W_{CW4}(t) = \frac{4e^{-t^2/\sigma}}{\sigma^2} \left(3 - \frac{12t^2}{\sigma} + \frac{4t^4}{\sigma^2} \right), \tag{17}$$

$$W_{H6}(t) = \beta^6 \left(\frac{[\cosh\,(\beta t)]^6 - 182[\cosh\,(\beta t)]^4 + 840[\cosh\,(\beta t)]^2 - 720}{[\cosh\,(\beta t)]^7} \right), \tag{18}$$
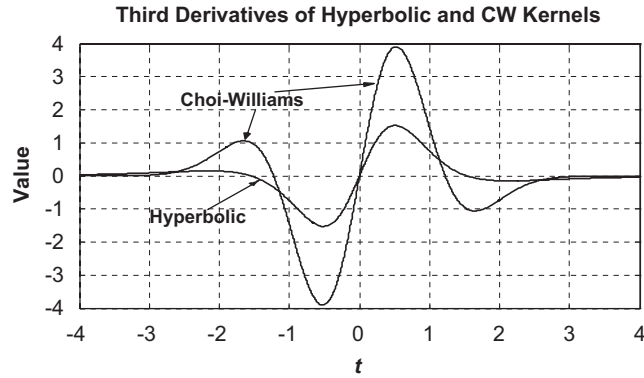
Fig. 2. Third-order derivatives of the first-order hyperbolic and CW kernels for $\beta = \sigma = 1$.

$$W_{CW6}(t) = \frac{8e^{-t^2/\sigma}}{\sigma^3}\left(-15 + \frac{90t^2}{\sigma} - \frac{60t^4}{\sigma^2} + \frac{8t^6}{\sigma^3}\right), \tag{19}$$

$$W_{H8}(t) = \beta^8\left(\frac{[\cosh(\beta t)]^8 - 1640[\cosh(\beta t)]^6 + 23,184[\cosh(\beta t)]^4 - 60,480[\cosh(\beta t)]^2 + 40,320}{[\cosh(\beta t)]^9}\right), \tag{20}$$

$$W_{CW8}(t) = \frac{16e^{-t^2/\sigma}}{\sigma^4}\left(105 - \frac{840t^2}{\sigma} + \frac{840t^4}{\sigma^2} - \frac{224t^6}{\sigma^3} + \frac{16t^8}{\sigma^4}\right), \tag{21}$$

$$W_{H10}(t) = \beta^{10}\left(\frac{\begin{array}{c}[\cosh(\beta t)]^{10} - 14,762[\cosh(\beta t)]^8 + 599,280[\cosh(\beta t)]^6 \\ -3,659,040[\cosh(\beta t)]^4 + 6,652,800[\cosh(\beta t)]^2 - 3,628,800\end{array}}{[\cosh(\beta t)]^{11}}\right), \tag{22}$$

$$W_{CW10}(t) = \frac{-32e^{-t^2/\sigma}}{\sigma^5}\left(945 - \frac{9450t^2}{\sigma} + \frac{12,600t^4}{\sigma^2} - \frac{5040t^6}{\sigma^3} + \frac{720t^8}{\sigma^4} - \frac{32t^{10}}{\sigma^5}\right). \tag{23}$$

By using similar mathematical techniques carried out in Eqs. (9) and (10), it is clear that the above functions meet the admissibility constraint imposed by Eq. (1) and hence they are admissible wavelets which are plotted in Figs. 3–6, respectively. By using Eq. (11), their normalisation constants are numerically given in Table 1.

It should be noted that a wavelet, as analogous to the complex exponential function in the Fourier transform, can be used to represent any signal by expressing it as a sum of products of the wavelet with its expansion coefficients [15,16]. Thus, the number of side lobes of a wavelet function, which determines the order of sub-harmonics used in the series sum, is important in representing signals since the more higher-order harmonics involved in the sum, the more accurate the approximation. As can be seen in Figs. 4 and 5, for the CW wavelet, there is a significant improvement of the eighth-order derivative with three side lobes to the sixth-order derivative with two side lobes. For the hyperbolic wavelet, there are no significant improvements in going from the sixth-order derivative to the eighth-order derivative whose numbers of side-lobes remain unchanged at two. From Fig. 5, the eighth-order derivative, and Fig. 6, the tenth-order derivative of the first-order hyperbolic and CW kernels, there are no significant improvements as their numbers of side-lobes remain unchanged. It should also be noted that the side-lobe and peak magnitude of both wavelets increase as the order increases. The larger is the peak magnitude, the more concentrated power is at the first harmonic in the expansion sum, and the more accurate is the signal approximation. Moreover, the larger is the side-lobe magnitude, the more accurate are the high-order sub-harmonic terms in the sum. From Figs. 3 to 6, it can also be suggested that the CW wavelets are better than the hyperbolic wavelets by having more side-lobes with larger magnitude. However, it was shown [9] that the second-order hyperbolic wavelet, which is the negative
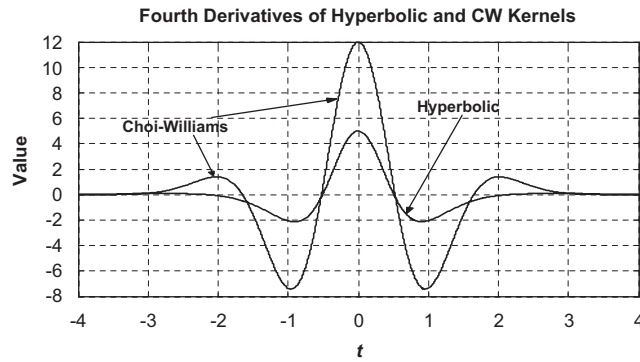
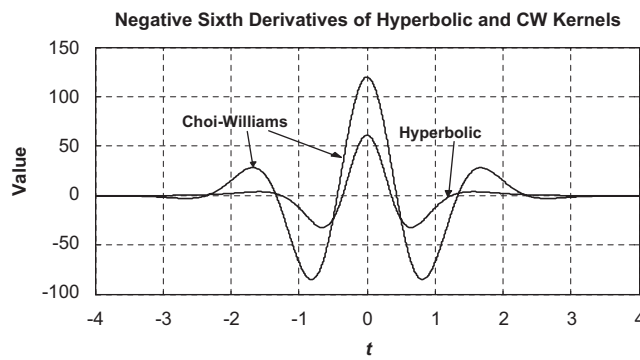Fig. 3. Fourth-order derivatives of the first-order hyperbolic and CW kernels for $\beta = \sigma = 1$.

Fig. 4. Negative sixth-order derivatives of the first-order hyperbolic and CW kernels for $\beta = \sigma = 1$.
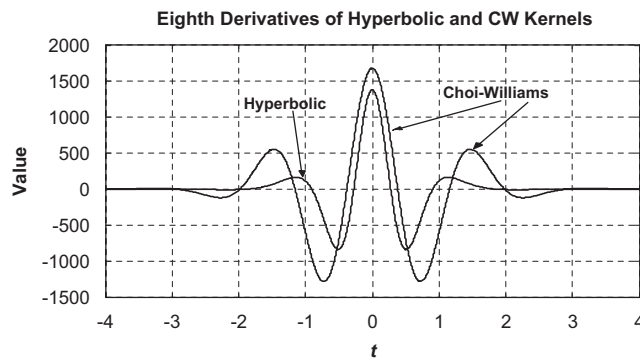

Fig. 5. Eighth-order derivatives of the first-order hyperbolic and CW kernels for $\beta = \sigma = 1$.

second-order derivative of the first-order hyperbolic kernel, is more effective than the CW second-order wavelet by having a finer scale resolution.

From Table 1, it is clear that the hyperbolic and CW wavelet normalisation constants second- up to tenth-order derivatives become significantly large as the derivative order increases. This means that high-order wavelets can finely concentrate their energy at the origin which results in relatively smaller side-lobe magnitude compared to the peak magnitude. This feature can be used to successfully expand certain sections of a wavelet power spectrum or time–frequency power spectrum to detect fine details or intensity changes in the input signal, of which amplification is also possible. By saying that, the tenth-order wavelet is more effective than the eighth-order wavelet because they possess an identical number of side lobes as explained earlier.
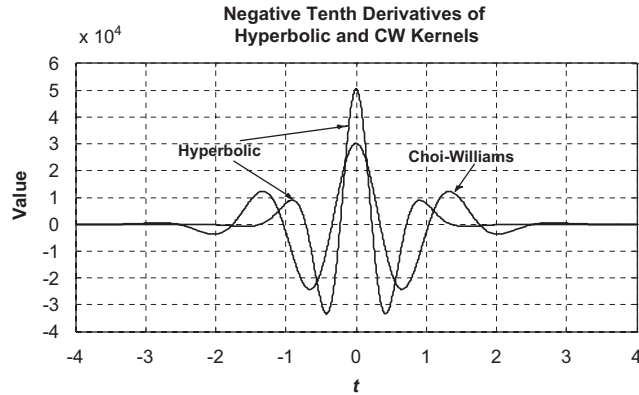
Fig. 6. Negative tenth-order derivatives of the first-order hyperbolic and CW kernels for $\beta = \sigma = 1$.

Table 1
Approximate normalisation constants of the hyperbolic (using first-order hyperbolic kernel) and CW high-order wavelets for $\beta = 1$ and $\sigma = 2$

	First-order Hyperbolic kernel	CW kernel, $\sigma = 2$
Second-order wavelet	0.97	1.153
Fourth-order wavelet	4.115	3.41
Sixth-order wavelet	45.53	17
Eighth-order wavelet	964.13	118.5
Tenth-order wavelet	33,311.44	1064.55

Time-domain studies on high-order hyperbolic and CW wavelets have been discussed in this section. For completeness, explicit expressions of the negative second-, fourth-, negative sixth-, eighth- and negative tenth-order wavelets of the nth-order hyperbolic kernel [5,9] are given by Eqs. (24)−(28), respectively

$$\psi_{\text{Hy}\_g2}(t) = (-1)n\beta^2[\text{sech}\,(\beta t)]^n\{n - (n+1)[\text{sech}\,(\beta t)]^2\}, \tag{24}$$

$$\psi_{\text{Hy}\_g4}(t) = n\beta^4\left(\frac{n^3}{[\cosh(\beta t)]^n} - \frac{2(n^3 + 3n^2 + 4n + 2)}{[\cosh(\beta t)]^{n+2}} + \frac{n^3 + 6n^2 + 11n + 6}{[\cosh(\beta t)]^{n+4}}\right), \tag{25}$$

$$\psi_{\text{Hy}\_g6}(t) = \frac{(-1)n\beta^6}{[\cosh(\beta t)]^n}\left(\begin{array}{l}[\cosh(\beta t)]^6 n^5 - [\cosh(\beta t)]^4(3n^5 + 15n^4 + 40n^3 + 60n^2 + 48n + 16) \\ +[\cosh(\beta t)]^2(3n^5 + 30n^4 + 125n^3 + 292n + 120) + \dfrac{270n^2}{[\cosh(\beta t)]^4} \\ -(n^5 + 15n^4 + 85n^3 + 225n^2 + 240n + 120)\end{array}\right), \tag{26}$$

$$\begin{aligned}\psi_{\text{Hy}\_g8}(t) = &\frac{n\beta^8}{[\cosh(\beta t)]^n} \\ &\times\left(\begin{array}{l}[\cosh(\beta t)]^8(n^7 + 28n^6 + 322n^5 + 1960n^4 + 6769n^3 + 13,132n^2 + 13,068n + 5040) \\ -[\cosh(\beta t)]^6(4n^7 + 84n^6 + 756n^5 + 3780n^4 + 11,256n^3 + 19,656n^2 + 18,224n + 6720) \\ +[\cosh(\beta t)]^4(6n^7 + 84n^6 + 546n^5 + 2100n^4 + 5040n^3 + 7392n^2 + 6000n + 2016) \\ -[\cosh(\beta t)]^2(4n^7 + 28n^6 + 112n^5 + 280n^4 + 448n^3 + 256n + 64) + n^7\end{array}\right),\end{aligned} \tag{27}$$

$$\psi_{\text{Hy\_}g10}(t) = \frac{(-1)n\beta^{10}}{[\cosh{(\beta t)}]^n}$$

$$\times \left(\begin{array}{l} -[\cosh{(\beta t)}]^{10}(n^9 + 45n^8 + 870n^7 + 9450n^6 + 63,273n^5 + 269,325n^4 \\ +723,680n^3 + 1,172,700n^2 + 1,026,576n + 362,880) \\ +[\cosh{(\beta t)}]^8(5n^9 + 180n^8 + 2850n^7 + 26,040n^6 + 150,885n^5 + 571,620n^4 \\ +1,402,900n^3 + 2,123,760n^2 + 1,769,760n + 604,800) \\ -[\cosh{(\beta t)}]^6(10n^9 + n^8 + 3330n^7 + 24,570n^6 + 118,692n^5 + 385,560n^4 \\ +832,640n^3 + 1,136,880n^2 + 874,848n + 282,240) \\ +[\cosh{(\beta t)}]^4(10n^9 + 480n^8 + 1590n^7 + 8820n^6 + 33,096n^5 + 85,680n^4 \\ +150,960n^3 + 170,320n^2 + 113,984n + 32,640) - [\cosh{(\beta t)}]^2(5n^9 + 45n^8 \\ +240n^7 + 840n^6 + 2016n^5 + 3360n^4 + 3840n^3 + 2880n^2 + 1280n + 256) + n^9 \end{array} \right). \qquad (28)$$

The nth-order hyperbolic wavelet normalisation constants can be explicitly found by using Eqs. (11) and (24)–(28), which extensively involve mathematical manipulations and therefore is beyond the scope of this paper. In addition, it is believed that they can be readily found once the kernel order n is specified. In general, high-order hyperbolic wavelets can be generated from their corresponding kernels by using the following formula:

$$\psi_{\text{Hyp}}(t) = (-1)^{(m\_\text{mod}\_2)} \frac{\text{d}^m[\Phi_{\text{Hyp}}(t)]}{(\text{d}t)^m}, \quad \text{for } m = 2, 4, 6, \ldots, \qquad (29)$$

where m is the wavelet order and m_mod_2 the modulo of m to 2, i.e. $(m = 2) \bmod 2 = 1$. If the modulo of m to 2 is an odd number (for cases of $m = 2, 6, 10, \ldots$) then negativity should be used so that the wavelet is concave-up and therefore has a positive peak at the origin.

As can be seen throughout this section, high-order kernel derivatives have been shown to be admissible wavelets. After completing time-domain studies of high-order wavelets, the answer to question 2 raised in Section 2 is that "negativity" is employed so that wavelets are concave-up functions. This means that their peaks will be positive and non-zero at the origin, which can also validate them as admissible kernels, providing that β and σ must be specifically chosen to meet kernel constraints 3 and 4 which impose that a function must possess a unity value under DC condition. Constraints 6 and 7 are also met by symmetrical wavelets since they are even functions and their odd-order derivative functions have been shown in this section, i.e. third-order derivative in Fig. 2, to vanish under DC conditions. Moreover, it is more important to note that the fourth-order kernel derivative is the second-order derivation (second-order Laplacian operator) of the second-order kernel derivative which means that recursively, the second-order kernel derivative can be considered as an admissible kernel if it is concave-up, and meets constraints 3 and 4 for some values of β and σ. Similarly, this recursive relation can be applied to admissible higher-order wavelets, and as the wavelet order m approaches infinity, there exist an infinite number of admissible kernels, which are generated from high-order wavelets, for Cohen's time–frequency power spectrum formula. It should also be stressed that concavity does not affect the wavelet expansion sum [15,16]. To satisfy constraints 3 and 4 so that admissible high-order wavelets possess a unity peak under DC conditions and therefore can be considered as admissible kernels, the parameters β and σ must be set to specific values, which are summarised in the following table for wavelet orders 2–10 (Table 2).

In this section, second- and higher-order derivatives of the first-order hyperbolic, CW and nth-order hyperbolic kernels have been discussed in which their expressions and normalisation constants are mathematically and numerically given. These functions have been graphically presented, and it is clear that they belong to a "crude" symmetrical wavelet group [9]. More importantly, high-order derivatives of admissible kernels have been shown to be admissible wavelets and it appears that these might perform better than the second-order hyperbolic and CW wavelets. The wavelet–kernel relationship has been explained via the meaning of positive concavity and kernels' even high-order derivative concepts.

Table 2
Approximate values of β and σ to generate admissible kernels from high-order hyperbolic and CW wavelets

Wavelet order	β	σ
Second	1 (exact)	2 (exact)
Fourth	$(1/5)^{1/4} \approx 0.669$	$\sqrt{12} \approx 3.46$
Sixth	$(1/61)^{1/6} \approx 0.5$	$120^{1/3} \approx 4.93$
Eighth	$(1/1385)^{1/8} \approx 0.404$	$1680^{1/4} \approx 6.4$
Tenth	$(1/50,521)^{1/10} \approx 0.339$	$30,240^{1/5} \approx 7.87$

4. Frequency-domain investigations of the hyperbolic and CW high-order wavelets by using high-order derivatives of the first-order hyperbolic and CW kernels

The Fourier transforms of the second-order hyperbolic and CW wavelets were given in Ref. [9] and will not be repeated here. This section extends the work reported in Refs. [9,14] by explicitly calculating parameters of the hyperbolic (using the first-order hyperbolic kernel) and CW high-order wavelets so that they can be used to analyse digital time series. Detailed definitions and meanings of these wavelet parameters were given in Refs. [9,14] and will not be repeated here. It was also shown in Sections 2 and 3 that high-order derivatives of the first-order hyperbolic and CW kernels are admissible wavelets, therefore, the terms "high-order derivatives" will be replaced by "high-order wavelets" from this point. In this section, the term "hyperbolic" kernel means "first-order hyperbolic" kernel, i.e. sech(βt), unless otherwise stated. It should also be noted that a wavelet's time-based interval, T, is dimensionless, while the sampling interval, $(\Delta t')$, of the digital input signal is dimensional. Thus a mapping method [9,14] was employed to consistently convert dimensional to non-dimensional quantities and vice versa. The method is given as [14]

$$t = \frac{2T}{N(\Delta t')} t',$$ (30)

where t and t' are non-dimensional and dimensional quantities, respectively.

An expression for a non-dimensional frequency f is obtained by taking the inverse of Eq. (30), yielding

$$f = \frac{N(\Delta t')}{2T} f', \quad \text{or} \quad \omega = \frac{\pi N(\Delta t')}{T} f'.$$ (31)

The non-dimensional Fourier transforms of the mth-order hyperbolic wavelets are explicitly given by

$$\hat{\psi}_{\text{Hyp}\_m}(\omega) = \frac{\pi \omega^m}{\beta} \text{sech}\left(\frac{\pi \omega}{2\beta}\right),$$ (32)

where $m = 2,4,6,8,10,\ldots$, is the even wavelet order.

4.1. Band-peak frequency

From Refs. [9,14], it should be noted that Eq. (32) is non-dimensional, thus, by using the relation

$$\omega = \frac{\pi N_{\text{Hyp}\_m}(\Delta t')}{T_{\text{Hyp}\_m}} f',$$

given by Eq. (31), the dimensional expression of the Fourier transform of the mth-order hyperbolic wavelet is explicitly given by

$$\hat{\psi}_{\text{Hyp}\_m}(f') = \frac{\pi \sqrt{a}}{\beta} \exp\left(-\frac{jN_{\text{Hyp}\_m}\pi f'(\Delta t')b'}{T_{\text{Hyp}\_m}}\right)\left(a\frac{N_{\text{Hyp}\_m}\pi f'(\Delta t')}{T_{\text{Hyp}\_m}}\right)^m \text{sech}\left(a\frac{\pi}{2\beta}\frac{N_{\text{Hyp}\_m}\pi f'(\Delta t')}{T_{\text{Hyp}\_m}}\right).$$ (33)

The wavelet dimensional band-peak frequency is found by equating its first derivative to zero and is explicitly given by

$$f'_p = \frac{2\beta m T_{\text{Hyp}\_m}}{a\pi^2 N_{\text{Hyp}\_m}(\Delta t')}. \tag{34}$$

As can be seen from Eq. (34), the hyperbolic wavelet band-peak frequency is directly proportional to the wavelet order m which suggests that high-order hyperbolic wavelets can be successfully used at high frequencies. The second-order hyperbolic wavelet ($m = 2$) has the lowest band-peak frequency which determines the lower operating frequency range of the hyperbolic wavelet family.

4.2. Aliasing

To avoid aliasing effects in sampling a wavelet non-dimensionally and the input signal dimensionally, the Nyquist criterion must be met. The wavelet minimum number of sampling points can be found by using the following formula [9,14] with the scale $a = 1$:

$$\alpha = \frac{\psi'_{a=1,b'}\left(f'_{N_y}\right)}{\psi'_{a=1,b'}\left(f'_p\right)}, \tag{35}$$

where $f'_{N_y} = 1/2(\Delta t')$ is the Nyquist frequency, f'_p the wavelet band-peak frequency and α the aliasing ratio, typically in the range of $0 < \alpha \leqslant 0.1$ (10%).

By using Eq. (35), and substituting $f'_{N_y} = 1/2(\Delta t')$ and f'_p [given by Eq. (34)] into Eq. (33), the mth-order hyperbolic wavelet minimum number of sampling points, N_{Hyp_m}, is the root of the following equation:

$$\alpha = \left(\frac{a N_{\text{Hyp}\_m}\pi^2}{4 T_{\text{Hyp}\_m}\beta m}\right)^m \frac{\cosh(m)}{\cosh\left(\frac{a N_{\text{Hyp}\_m}\pi^2}{4 T_{\text{Hyp}\_m}\beta}\right)}. \tag{36}$$

When m approaches infinity, from Eq. (36), N_{Hyp_m} is the root of the following equation:

$$\alpha \cosh\left(\frac{a N_{\text{Hyp}\_m}\pi^2}{4 T_{\text{Hyp}\_m}\beta}\right) = \frac{\cosh(m)}{m^m} \xrightarrow{m\to\infty} 0, \tag{37}$$

in which there are no solutions to N_{Hyp_m}. From Eq. (37), it might be suggested that infinitely high-order hyperbolic wavelets are not practically useful, leading to a trade-off between kernel and wavelet performance, as reported in Ref. [5], in which the larger β is, the more effective cross-term-suppression is the hyperbolic kernel, but the coarser is its wavelet scale resolution. In general, it should be noted that once m, which must be different from zero, is specified, the wavelet one-sided time-based interval T_{Hyp_m} can be estimated, and hence its minimum number of sampling points by applying a graphical method [9] to Eq. (36).

4.3. Scale limit

Scales are inversely proportional to frequencies in the frequency domain. For each wavelet, there exists a maximum scale number that it can display. The larger is the scale limit, the more effective is the wavelet for broad-spectrum analyses. The maximum scale number used for a wavelet is determined based on the number of wrapped-around points or end-points of the input signal since these points do not provide useful information. From Refs. [9,14], the number of wrapped-around points, as a function of the scale a, at one end is approximately given as

$$N_{\text{wrap}}(a) \approx \frac{a(N - 1)}{2}. \tag{38}$$

To estimate the maximum scale number of a wavelet, η is introduced as a fraction of the number of wrapped-around points $N_{\mathrm{wrap}}(a)$ [given by Eq. (38)] and $M = 2^k$, the number of input data points into the wavelet, to obtain [9,14]

$$\frac{a_{\max}(N_{\mathrm{Hyp\_}m} - 1)/2}{2^k} \leqslant \frac{\eta}{2}, \quad \text{and} \quad \eta = \frac{N_{\mathrm{wrap}}(a)}{M}. \tag{39}$$

Thus, for a given value of $N_{\mathrm{Hyp\_}m}$, the wavelet scale limit can be found by using Eq. (39). To obtain a fast calculation, M should be a power of two which means k should be an integer. It should also be noted that the smaller M is, the more efficient is the wavelet.

4.4. Scale resolution

The scale resolution of the hyperbolic second-order wavelet was studied in detail in Refs. [9,14] and will not be repeated here. This section gives an explicit formula for the scale resolution of the mth-order hyperbolic wavelet or hyperbolic wavelet family. The scale resolution is defined as the distance between band-peak frequencies of two adjacent wavelets

$$\lambda = \frac{\hat{\psi}(a\omega_p)}{\hat{\psi}(a\omega_p + \omega_d)}, \tag{40}$$

where λ is the scale resolution ratio, typically in the range of $0 \leqslant \lambda \leqslant 1$. Substituting Eq. (34) into Eq. (32), the scale resolution of the hyperbolic wavelet order m is explicitly given as

$$\lambda = \frac{(2\beta m)^m}{\cosh(m)} \frac{\cosh\left(\dfrac{2m\beta + \pi\omega_d}{2\beta}\right)}{(2m\beta + \pi\omega_d)^m}. \tag{41}$$

It is advantageous for the hyperbolic wavelet family to possess explicit formulas for its band-peak frequency, minimum number of scales and scale resolution, which allow easier theoretical and simulation investigations, and clearly review properties of different family members when the order m varies. Some approximations can be obtained.

- *For m approaching infinity*
  The wavelet scale resolution cannot be estimated from Eq. (41). In fact, the ratio λ must be set to unity so that the equation remains correct. Thus, it is not practical to increase σ to infinity which agrees with what was discussed in Ref. [5].
- *For other non-zero values of m*
  The scale resolution can be graphically obtained by using a graphical method in 3-D which means that, from Eq. (41), the intersection(s) of two planes: λ and

$$\frac{(2\beta m)^m}{\cosh(m)} \frac{\cosh\left(\dfrac{2m\beta + \pi\omega_d}{2\beta}\right)}{(2m\beta + \pi\omega_d)^m},$$

are the approximate values of the wavelet scale resolution(s). To obtain a finite solution to the hyperbolic fourth-order scale resolution, λ must be set to unity and this condition is applied to all members of the hyperbolic wavelet family. It should also be noted that the smaller β is, the higher is the wavelet order m, which is shown in Section 6.

A total number of wavelet scales j_{max}, as a function of ω_d, can also be estimated by using the following formula [9,14]:

$$j_{\max} = \frac{\ln(a_{\max})}{\ln\left(\dfrac{\omega_{p(1)}}{\omega_{p(1)} - \omega_d}\right)} + 1,$$ (42)

where $\omega_{p(1)}$ is the wavelet non-dimensional band-peak frequency at $a = 1$.

From Eq. (42), the total number of scales can be explicitly obtained once a_{max} is given. The non-dimensional band-peak frequency $\omega_{p(1)}$ can also be explicitly obtained by multiplying the factor $\pi N(\Delta t'/T)$ to the dimensional band-peak frequencies given by Eq. (34) of the hyperbolic wavelet, and by Eqs. (51) and (52) of the CW wavelet. The fourth-order hyperbolic and CW wavelet total numbers of scales are numerically estimated in Section 6.

5. CW high-order wavelets

In this section, the CW fourth-order wavelet will be studied in detail in which its parameters are explicitly given in Section 5.1 along with some useful approximations for extreme values of σ, and numerically estimated in Section 6. The CW sixth-, eighth- and tenth-order wavelet parameters cannot be obtained because of the involvement of extensive mathematical manipulations which is beyond the scope of this paper. However, their Fourier transforms are briefly given by

$$\hat{\psi}_{\mathrm{CW4}}(\omega) = \frac{\sqrt{\pi\sigma}\exp\left(\dfrac{-\sigma\omega^2}{4}\right)}{\sigma^2}\left(\sigma^2\omega^2 + 12\sigma\omega - 2\sigma + 12\right),$$ (43)

$$\hat{\psi}_{\mathrm{CW6}}(\omega) = \frac{\sqrt{\pi\sigma}\exp\left(\dfrac{-\sigma\omega^2}{4}\right)}{\sigma^3}\left(\sigma^3\omega^3 + 30\sigma^2\omega^2 - 6\sigma\omega(\sigma - 30) - 60\sigma + 120\right),$$ (44)

$$\hat{\psi}_{\mathrm{CW8}}(\omega) = \frac{\sqrt{\pi\sigma}\exp\left(\dfrac{-\sigma\omega^2}{4}\right)}{\sigma^4}\left(\begin{array}{c}\sigma^4\omega^4 + 56\sigma^3\omega^3 - 12\sigma^2\omega^2(\sigma - 70) \\ -336\sigma\omega(\sigma - 10) + 12\sigma^2 - 1680\sigma + 1680\end{array}\right),$$ (45)

$$\hat{\psi}_{\mathrm{CW10}}(\omega) = \frac{\sqrt{\pi\sigma}\exp\left(\dfrac{-\sigma\omega^2}{4}\right)}{\sigma^5}\left(\begin{array}{c}\sigma^5\omega^5 + 90\sigma^4\omega^4 - 20\sigma^3\omega^3(\sigma - 126) - 360\sigma^2\omega^2(3\sigma - 70) \\ +60\sigma\omega(\sigma^2 - 252\sigma + 1260) + 1080\sigma^2 - 50,400\sigma + 30,240\end{array}\right).$$ (46)

The relation $\omega = \pi N(\Delta t')f'/T$ is used to convert a non-dimensional frequency ω to the dimensional frequency f', yielding the dimensional expressions of CW wavelets as

$$\hat{\psi}_{\mathrm{CW4}}(f') = \frac{\sqrt{a\pi\sigma}\exp\left[\dfrac{-\sigma}{4}\left(a\dfrac{\pi N_{\mathrm{CW4}}(\Delta t')f'}{T_{\mathrm{CW4}}}\right)^2\right]}{\sigma^2}\exp\left(-\mathrm{j}\dfrac{N_{\mathrm{CW4}}\pi(\Delta t')f'b'}{T_{\mathrm{CW4}}}\right)$$
$$\times\left[\sigma^2\left(a\dfrac{\pi N_{\mathrm{CW4}}(\Delta t')f'}{T_{\mathrm{CW4}}}\right)^2 + 12\sigma\left(a\dfrac{\pi N_{\mathrm{CW4}}(\Delta t')f'}{T_{\mathrm{CW4}}}\right)^2 - 2\sigma + 12\right],$$ (47)

$$\hat{\psi}_{\text{CW6}}(f') = \frac{\sqrt{a\pi\sigma}\exp\left(\dfrac{-\sigma}{4}\left(a\dfrac{\pi N_{\text{CW6}}(\Delta t')f'}{T_{\text{CW6}}}\right)^2\right)}{\sigma^3}\exp\left(-j\frac{N_{\text{CW6}}\pi(\Delta t')f'b'}{T_{\text{CW6}}}\right)\left(\sigma^3\left(a\frac{\pi N_{\text{CW6}}(\Delta t')f'}{T_{\text{CW6}}}\right)^3\right.$$
$$\left. +30\sigma^2\left(a\frac{\pi N_{\text{CW6}}(\Delta t')f'}{T_{\text{CW6}}}\right)^2 - 6\sigma(\sigma-30)\left(a\frac{\pi N_{\text{CW6}}(\Delta t')f'}{T_{\text{CW6}}}\right) - 60\sigma + 120\right), \tag{48}$$

$$\hat{\psi}_{\text{CW8}}(\omega) = \frac{\sqrt{\pi\sigma}\exp\left(-0.25\sigma\left(\dfrac{\pi N_{\text{CW8}}(\Delta t')f'}{T_{\text{CW8}}}\right)^2\right)}{\sigma^4}$$
$$\times\left[\begin{array}{l}\sigma^4\left(a\dfrac{\pi N_{\text{CW8}}(\Delta t')f'}{T_{\text{CW8}}}\right)^4 + 56\sigma^3\left(a\dfrac{\pi N_{\text{CW8}}(\Delta t')f'}{T_{\text{CW8}}}\right)^3 - 12\sigma^2\left(a\dfrac{\pi N_{\text{CW8}}(\Delta t')f'}{T_{\text{CW8}}}\right)^2(\sigma-70) \\[2mm] -336\sigma(\sigma-10)\left(a\dfrac{\pi N_{\text{CW8}}(\Delta t')f'}{T_{\text{CW8}}}\right) + 12\sigma^2 - 1680\sigma + 1680\end{array}\right], \tag{49}$$

$$\hat{\psi}_{\text{CW10}}(\omega) = \frac{\sqrt{\pi\sigma}\exp\left(-0.25\sigma\left(\dfrac{\pi N_{\text{CW10}}(\Delta t')f'}{T_{\text{CW10}}}\right)^2\right)}{\sigma^5}$$
$$\left[\begin{array}{l}\sigma^5\left(a\dfrac{\pi N_{\text{CW10}}(\Delta t')f'}{T_{\text{CW10}}}\right)^5 + 90\sigma^4\left(a\dfrac{\pi N_{\text{CW10}}(\Delta t')f'}{T_{\text{CW10}}}\right)^4 \\[2mm] -20\sigma^3\left(a\dfrac{\pi N_{\text{CW10}}(\Delta t')f'}{T_{\text{CW10}}}\right)^3(\sigma-126) - 360\sigma^2\omega^2(3\sigma-70) \\[2mm] +60\sigma(\sigma^2-252\sigma+1260)\left(a\dfrac{\pi N_{\text{CW10}}(\Delta t')f'}{T_{\text{CW10}}}\right) + 1080\sigma^2 - 50,400\sigma + 30,240\end{array}\right]. \tag{50}$$

5.1. CW fourth-order wavelet

The hyperbolic and CW fourth-order wavelets were graphically presented in Section 3 in the time-domain. Their frequency domain representations are also given in Fig. 7 in which the CW fourth-order wavelet exhibits a "negative" frequency power spectrum for "negative" frequencies while the CW second-order wavelet possesses a positive frequency spectrum for the whole frequency range which can be suggested that high-order hyperbolic wavelets might be useful for optical pattern recognition using a joint transform correlator [18]. The hyperbolic second- and fourth-order wavelets possess positive spectra whose peak positions might also affect the optical correlator performance. However, this paper is devoted to studies of high-order hyperbolic and CW wavelets and therefore performance of optical joint transform correlators will be addressed in a separate publication. The CW fourth-order wavelet parameters are explicitly given in this section, and also numerically estimated in Section 6 for $\beta = 1/\sigma = 0.5$. It should be noted that there might exist different numerical values for a wavelet parameter in which the largest is chosen. However, for a wavelet, its time-based interval T is unique.

5.1.1. Band-peak frequency

Similar to Section 4.1, after some mathematical manipulations, the dimensional wavelet band-peak frequencies are given by

$$f'_{p1} = \frac{D_0 T_{\text{CW4}}}{a\pi N_{\text{CW4}}(\Delta t')}, \tag{51}$$
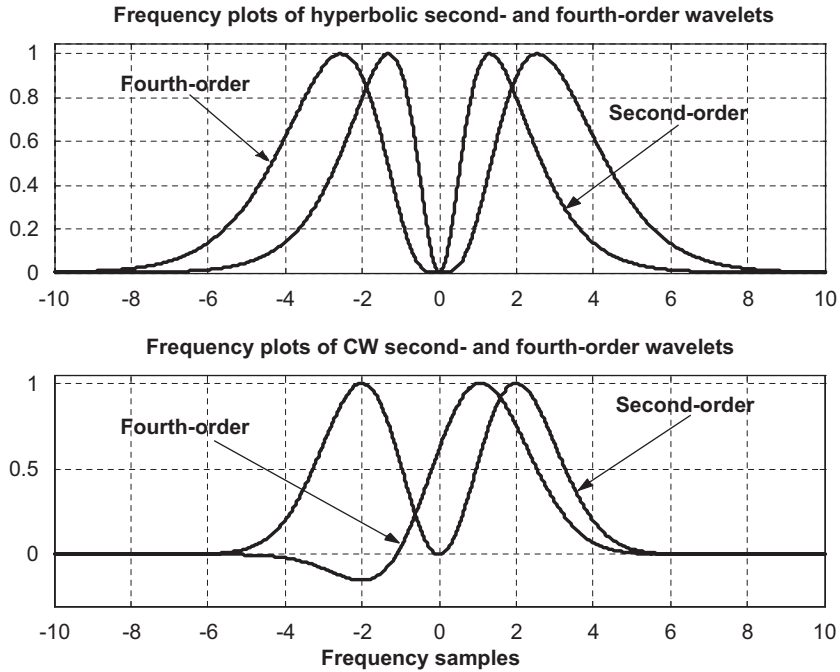
Fig. 7. Normalised frequency-domain representations of the hyperbolic and CW fourth-order wavelets for $\beta = \sigma = 1$.

where

$$D_0 = \frac{1}{\sigma}\left((2c - 40)^{1/3} - 4 + \frac{2(\sigma + 6)}{(2c - 40)^{1/3}}\right),$$

$$f'_{p2,3} = \frac{T_{CW4}}{a\pi N_{CW4}(\Delta t')}\sqrt{(D_1)^2 \pm \frac{3}{4}(D_2)^2}, \tag{52}$$

where

$$|c| = \sqrt{2(\sigma^3 + 18\sigma^2 + 108\sigma + 16)},$$

$$D_1 = \frac{1}{\sigma}\left(\frac{(2c - 40)^{1/3}}{2} + \frac{\sigma + 6}{(2c - 40)^{1/3}} + 4\right), \quad \text{and} \quad D_2 = \frac{1}{\sigma}\left((2c - 40)^{1/3} - \frac{2(\sigma + 6)}{(2c - 40)^{1/3}}\right).$$

5.1.2. Aliasing

Three different minimum numbers of samplings points can be obtained from three different band-peak frequencies given by Eqs. (51) and (52). The first minimum number of sampling points, obtained by using f'_{p1}, can be found by applying the graphical method to the following expression:

$$\alpha = \frac{(D^2 + 12D - 2\sigma + 12)\exp\left(-D^2/4\right)}{\left[\left(\frac{N_{CW4\_1}\pi\sigma}{2T_{CW4}}\right)^2 + \frac{6N_{CW4\_1}\pi\sigma}{T_{CW4}} - 2\sigma + 12\right]\exp\left(-\frac{N_{CW4\_1}^2\pi^2\sigma}{16(T_{CW4})^2}\right)}, \tag{53}$$

where

$$D = \frac{1}{\sigma}\left(\frac{(2c - 40)^{1/3}}{2} - \frac{\sigma + 6}{(2c - 40)^{1/3}} + 4\right).$$

The identical second and third numbers of sampling points, found by using f'_{p2} and f'_{p3}, are given by

$$\alpha = \frac{\left[\left(\frac{N_{\text{CW4\_2}}\pi\sigma}{2T_{\text{CW4}}}\right)^2 + \frac{6N_{\text{CW4\_2}}\pi\sigma}{T_{\text{CW4}}} - 2\sigma + 12\right]\exp\left(-\frac{(N_{\text{CW4\_2}}\pi)^2\sigma}{16T_{\text{CW4}}^2}\right)}{\left[\sigma^2\left(D_1^2 + \frac{3D_2^2}{4}\right) + 12\sigma\sqrt{D_1^2 + \frac{3D_2^2}{4}} - 2\sigma + 12\right]\exp\left(-\frac{\sigma\sqrt{4D_1^2 + 3D_2^2}}{8}\right)}. \tag{54}$$

The following approximations are obtained for σ approaching zero and infinity.

- *For σ approaching zero*
  We obtain, $|D_{0\_\text{small}}| = |D_{1\_\text{small}}| = |D_{2\_\text{small}}| = |D_{\text{small}}| \to \infty$, and $c_{\text{small}} \approx 4\sqrt{2}$. Moreover, with a known wavelet order, the time-based interval T_{CW4} can be graphically estimated. The wavelet band-peak frequencies therefore become

$$f'_{p1\_\text{small}} \approx \frac{2.17T_{\text{CW4}}}{a\pi N_{\text{CW4}}(\Delta t')}, \tag{55}$$

$$f'_{p2\_\text{small}} \approx \frac{16T_{\text{CW4}}}{a\pi N_{\text{CW4}}(\Delta t')}, \quad \text{and} \quad f'_{p3\_\text{small}} \approx \frac{4.22T_{\text{CW4}}}{a\pi N_{\text{CW4}}(\Delta t')}. \tag{56}$$

The aliasing ratios, given by Eqs. (53) and (54), become

$$\exp\left(-\frac{N_{\text{CW4\_1}}^2\pi^2\sigma}{16T_{\text{CW4}}^2}\right) \approx \frac{0.1106544012 \times 10^{-7}}{\alpha_{1\_\text{small}}}, \tag{57}$$

$$\alpha_{2,3\_\text{small}} \approx \exp\left(-\frac{(N_{\text{CW4\_2}}\pi)^2\sigma}{16T_{\text{CW4}}^2}\right), \tag{58}$$

in which the wavelet minimum numbers of sampling points can be numerically estimated by using its approximate time-based interval T_{CW4}. From Eq. (58), it should also be noted that, when σ becomes infinitely small, its right-hand side becomes unity which also forces the left-hand side, α, to unity, yielding no solutions to $N_{\text{CW4\_2}}$. Thus, Eq. (57) should be mainly used to numerically estimate the minimum number of sampling points under this condition.

- *For σ approaching infinity*
  We obtain, $c_{\text{large}} \approx \sigma\sqrt{2\sigma} \to \infty$, and $D_{0\_\text{large}} = D_{1\_\text{large}} = D_{2\_\text{large}} = D_{\text{large}} \to 0$, yielding near DC band-peak frequencies [Eqs. (51) and (52)] and infinite minimum numbers of sampling point [from Eqs. (53) and (54)], which are not practically useful. Thus, for practical purposes, this condition should not be employed as also discussed in Ref. [5].

5.1.3. Scale limit

For a chosen value of η, the wavelet scale limit a_{max} can be numerically estimated (Section 6) by using Eqs. (38) and (39) once the minimum number of sampling points is estimated by using Eqs. (53) and (54), respectively.

5.1.4. Scale resolution

The non-dimensional band-peak frequency, which must be used to estimate the wavelet scale resolution, is found by multiplying the factor $\pi N(\Delta t')/T$ to the wavelet band-peak frequencies given by Eqs. (51) and (52), yielding

$$\omega_{p1} = \frac{D_0}{a}, \tag{59}$$

and

$$\omega_{p2,3} = \frac{1}{a}\sqrt{D_1^2 \pm \frac{3}{4}D_2^2} = \frac{E}{a}, \tag{60}$$

where $E = \sqrt{D_1^2 \pm \frac{3}{4}D_2^2}$.

By using Eqs. (59) and (60), the wavelet scale resolutions, obtained by using its three different band-peak frequencies, are roots of the following Eqs. (61)−(63), respectively,

$$\lambda = \frac{2\left(cC^{1/3} + 4C^{1/3} + \sigma C^{1/3} + 2C^{2/3} + 4c - 8 + 2\sigma^2 + 24\sigma + 4\sigma C^{1/3}\right)}{A + 4\sigma^2\omega_{d1}C^{1/3} + 4\sigma\omega_{d1}c - 80\sigma\omega_{d1} + \sigma^2\omega_{d1}^2 C^{2/3} + 2C^{1/3}c + 8c}$$
$$\times \exp\left(\frac{\omega_{d1}(4\sigma + \sigma\omega_{d1}C^{1/3} - 8C^{1/3} + 24 + 2C^{1/3})}{4C^{1/3}}\right), \tag{61}$$

$$\lambda = \frac{(\sigma^2 E_1^2 + 12\sigma E_1 - 2\sigma + 12)\exp\left(\dfrac{(\omega_{d2} + 2E_1)\sigma\omega_{d2}}{4}\right)}{\sigma^2\omega_{d2}^2 + 2\sigma\omega_{d2}(E_1\sigma + 6) + E_1^2 + 12\sigma E_1 - 2\sigma + 12}, \tag{62}$$

where $E_1 = \sqrt{D_1^2 \pm \frac{3}{4}D_2^2}$,

$$\lambda = \frac{(\sigma^2 E_2^2 + 12\sigma E_2 - 2\sigma + 12)\exp\left(\dfrac{(\omega_{d3} + 2E_2)\sigma\omega_{d3}}{4}\right)}{\sigma^2\omega_{d3}^2 + 2\sigma\omega_{d3}(E_2\sigma + 6) + E_2^2 + 12\sigma E_2 - 2\sigma + 12}, \tag{63}$$

where

$$E_2 = \sqrt{D_1^2 - \tfrac{3}{4}D_2^2}, \quad C = 2c - 40,$$

and

$$A = 4\sigma\omega_d C^{1/3}(6 + C^{1/3}) - 16 + 4C^{2/3} + 2\sigma C^{2/3} + 8C^{1/3} + 8\sigma C^{1/3} + 48\sigma + 4\sigma^2.$$

Similar approximations are obtained to numerically estimate the scale resolutions.

- *For σ approaching zero*

  We obtain, $|c_{small}| \approx 4\sqrt{2}$, $|D_{0\_small}| = |D_{1\_small}| = |D_{2\_small}| = |D_{small}| = E_{1\_small} = E_{2\_small} \to \infty$, $C_{small} \approx -28.7$, $|C^{1/3}| \approx 3.06$, $|C^{2/3}| \approx 9.37$ and $|A_{small}| \approx -16 + 4C^{1/3} + 8C^{1/3} \approx 46$. By using these values, Eq. (61) becomes

  $$\lambda \approx 0.9997\exp(18.26\omega_{d1\_small}), \tag{64}$$

  which yields a fine scale resolution of $\omega_{d1\_small} \approx 2 \times 10^{-5}$. Under this condition, Eqs. (62) and (63) do not yield solutions to the wavelet scale resolutions.

- *For σ approaching infinity*

  We obtain

  $$c_{large} \approx \sigma\sqrt{2\sigma}, \quad D_{0\_large} = D_{1\_large} = D_{2\_large} = D_{large} = E_1 = E_2 \to 0,$$

  yielding

  $$C_{large} \approx 2c, (C_{large})^{2/3} \sim 1.26\sigma, (C_{large})^{1/3} \approx 1.12\sigma^{1/2},$$

and $A_{\mathrm{large}} \approx 4\sigma^2$. Thus, Eq. (61) becomes

$$\lambda \approx \frac{10.52 \, \exp(5.82\sigma^{1/2} + 0.9\omega_{d1\_\mathrm{large}}\sigma)}{5.66\sigma^{1/2} + 1.26\sigma\omega_{d1\_\mathrm{large}}^2}. \tag{65}$$

From Eq. (65), the scale resolution can be numerically estimated by locating the intersection(s) of two functions: $y_1 = (5.66\sigma^{1/2} + 1.26\sigma\omega_{d1\_\mathrm{large}}^2)\lambda$ and $y_2 = 10.52 \exp(5.82\sigma^{1/2} + 0.9\omega_{d1\_\mathrm{large}}\sigma)$. It should be noted that as σ increases, solutions to $\omega_{d1\_\mathrm{large}}$ are more difficult to obtain because y_2 approaches infinity for $\sigma \geqslant 10$. Eqs. (62) and (63) also do not yield solutions to the scale resolutions.

- *For other values of σ*
  The wavelet's first scale resolution can be found by using Eq. (61) and is plotted against σ and λ in Fig. 8 for $2 \times 10^{-3} \leqslant \sigma \leqslant 10$, and in Fig. 10 for $10 \leqslant \sigma \leqslant 50$. For $\sigma > 50$, the scale resolution becomes very coarse and approaches unity for large values of σ. The second and third scale resolutions are numerically estimated by using Eqs. (62) and (63), yielding

$$\lambda \approx \frac{\exp\left(\dfrac{(\omega_{d2} + 11.6)\omega_{d2}}{2}\right)}{4\omega_{d2}^2 + 70.53\omega_{d2} + 181.43}, \tag{66}$$

which does not yield a solution to ω_{d2}, and

$$\lambda \approx \frac{\exp\left(\dfrac{(\omega_{d3} + 7.5)\omega_{d3}}{2}\right)}{4\omega_{d3}^2 + 54\omega_{d3} + 112.206}, \tag{67}$$

which does not yield a solution to ω_{d3}.
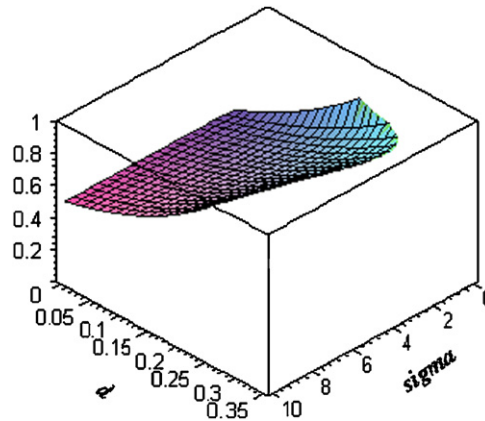
Fig. 8. CW fourth-order wavelet scale resolution ("d" axis) for $2 \times 10^{-3} \leqslant \sigma \leqslant 10$ and $0 \leqslant \lambda \leqslant 1$ (vertical axis).
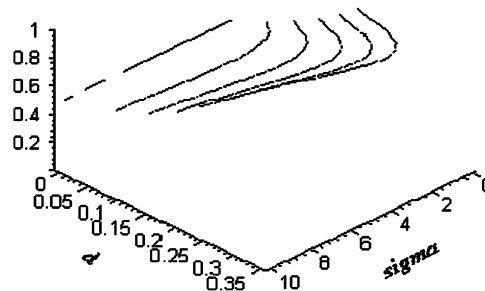

Fig. 9. Contour plot of Fig. 8, λ is vertical axis. The scale resolution can be read across to "d" axis on graph.
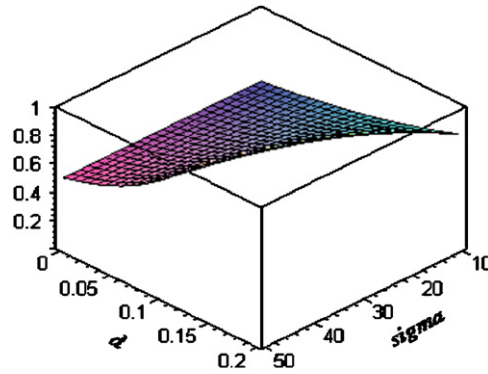
Fig. 10. CW fourth-order wavelet scale resolution for $10 \leqslant \sigma \leqslant 50$ and $0 \leqslant \lambda \leqslant 1$.
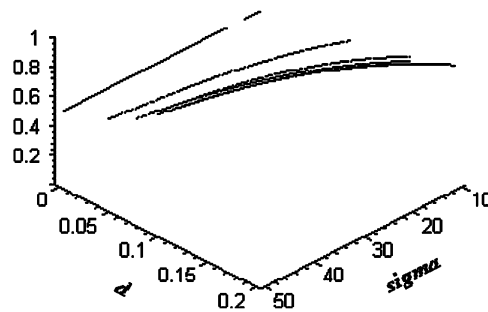

Fig. 11. Contour plot of Fig. 10. The scale resolution can be read across to the "d" axis on graph.

Table 3
Approximate parameter values of the CW fourth-order wavelet

Parameter	σ approaching zero	σ approaching infinity	Other values
Band-peak frequency, f_p	Eqs. (55) and (56)	Zero (DC)	Given in Section 6
Minimum number of sampling points, N_{CW4}	Eqs. (53) and (54)	Depending on T_{CW4}	
Scale limit, a_{max}	Depending on N_{CW4}		
Scale resolution, ω_d	2×10^{-5}	—	0.32 at $\sigma \approx 3$, and 0.15 at $\sigma \approx 10$

For the CW fourth-order wavelet, as can be seen in Figs. 9 and 10, its coarsest scale resolution of approximately 0.32 is obtained at $\sigma \approx 3$. For $10 \leqslant \sigma \leqslant 50$, the scale resolution becomes finer with the coarsest of about 0.15 (Fig. 11) at $\sigma \approx 10$. Thus, it is clear that as σ increases (β decreases), the scale resolutions of the CW high-order wavelets decrease, and become finer. This is consistent with what was reported in Refs. [5,9,19] in which increasing σ (decreasing β for the hyperbolic kernel) reduces the CW kernel's effectiveness in suppressing cross terms and noise robustness, but improves its auto-term support and wavelet scale resolutions.

Table 3 summarises numerical values of the CW fourth-order wavelet for σ approaching zero and infinity.

6. Numerical example

In this section, minimum numbers of sampling points, band-peak frequencies, scale limits, scale resolutions, and maximum numbers of scales of the fourth-order CW and hyperbolic wavelets are numerically estimated, given the sampling time interval ($\Delta t'$) = 0.2 ms, aliasing ratio $\alpha = 0.01$ (1%), $\beta = 0.5$, $\sigma = 2$, and time-based interval T which can be graphically estimated for each wavelet. Comparisons among Morlet, second- and fourth-order hyperbolic and CW wavelets are also given. From Fig. 3, the hyperbolic and CW fourth-order

wavelet time-based intervals are graphically estimated as $T_{\mathrm{Hyp\_4}} \approx T_{\mathrm{CW4}} \approx 3$. From Eq. (36), the minimum numbers of sampling points for the fourth-order hyperbolic wavelet ($m = 4$) are the roots of the following equation:

$$0.01 = \left(\frac{N_{\mathrm{Hyp\_4}} \times \pi^2}{4 \times T_{\mathrm{Hyp\_4}} \times \beta \times 4} \right)^4 \frac{\cosh(4)}{\cosh \left(\frac{N_{\mathrm{Hyp\_4}} \times \pi^2}{4 \times T_{\mathrm{Hyp\_4}} \times \beta} \right)}, \tag{68}$$

approximately yielding two solutions to $N_{\mathrm{Hyp\_4}}$ of 1 and 4, of which $N_{\mathrm{Hyp\_4}} \approx 4$ is chosen. From Eq. (34), the hyperbolic fourth-order wavelet band-peak frequency is given by

$$f'_{\mathrm{Hyp\_4}} = \frac{2 \times 0.5 \times 4 \times 3}{a\pi^2 \times 4 \times (0.2 \times 10^{-3})} \approx \frac{1521.36}{a}. \tag{69}$$

For the CW fourth-order wavelet, the minimum numbers of sampling points can be obtained by using Eqs. (53) and (54). For $\sigma = 2$, we obtain, $D \approx 0.68$, $D_0 \approx 2.79$, $D_1 \approx 4.4$ and $D_2 \approx -2.64$, hence, Eq. (53) becomes

$$0.01 = \frac{14.8}{(1.1N_{\mathrm{CW4\_1}}^2 + 12.56N_{\mathrm{CW4\_1}} + 8) \exp(-0.137N_{\mathrm{CW4\_1}}^2)}, \tag{70}$$

which does not yield a solution to $N_{\mathrm{CW4\_1}}$. From Eq. (54), the second and third minimum numbers of sampling points are roots of Eq. (71)

$$0.01 = 0.053(1.1N_{\mathrm{CW4\_2}}^2 + 12.56N_{\mathrm{CW4\_2}} + 8) \exp(-0.137N_{\mathrm{CW4\_2}}^2), \tag{71}$$

which yields an approximate solution of $N_{\mathrm{CW4\_2}} \approx 7$. From Eqs. (51) and (52), the CW fourth-order wavelet band-peak frequencies are therefore given as

$$f'_{\mathrm{CW}p1} = \frac{2.79 \times 3}{a \times 3.14 \times 7 \times 0.2 \times 10^{-3}} \approx \frac{1904}{a}, \tag{72}$$

$$f'_{\mathrm{CW}p2} \approx \frac{3}{a \times 3.14 \times 7 \times 0.2 \times 10^{-3}} \sqrt{(4.4)^2 \pm \frac{3}{4}(2.64)^2} \approx \frac{3384}{a}, \quad \text{and} \quad f'_{\mathrm{CW}p3} \approx \frac{2565.5}{a}, \tag{73}$$

of which $f'_{\mathrm{CW}p1} \approx 1904/a$ and $f'_{\mathrm{CW}p2} \approx 3384/a$ are chosen as its minimum and maximum band-peak frequencies, respectively.

To numerically estimate a wavelet maximum scale number $a_{\max}$, it should be noted that band-peak frequencies can also be scaled down to approximately 30 Hz, which can be increased or decreased depending upon a particular application [14]. From Eq. (69), the hyperbolic wavelet maximum scale number is numerically given as

$$a_{\max}^{\mathrm{Hyp4}} = \frac{1521.36}{30} \approx 51. \tag{74}$$

From Eqs. (72) and (73), the maximum scale numbers of the CW fourth-order wavelet are numerically given as

$$a_{\max 1}^{\mathrm{CW4}} = \frac{1904}{30} \approx 63.5, \quad \text{and} \quad a_{\max 3}^{\mathrm{CW4}} = \frac{2565.5}{30} \approx 85.5. \tag{75}$$

By using Eqs. (38) and (39), respectively, for the hyperbolic and CW fourth-order wavelets and assuming that $\eta = \frac{1}{3}$ [Eq. (38)], their minimum numbers of input data points M can be numerically estimated. For the hyperbolic fourth-order wavelet, by using $a_{\max}^{\mathrm{Hyp4}} \approx 51$ from Eq. (74) and $N_{\mathrm{Hyp4}} \approx 4$ from Eq. (68), its minimum number of data points M_{Hyp4} is approximately given as

$$M_{\mathrm{Hyp4}} = 2^k = \frac{51 \times (4 - 1)}{1/3} \geqslant 459, \tag{76}$$

which should be chosen as $M_{\text{Hyp4}} = 512$, yielding $k_{\text{Hyp4}} = 9$ for a fast calculation. It should also be noted that since $N_{\text{Hyp4}} \approx 4$ is small which might not be sufficient to sample the wavelet, a higher value might be chosen to improve its sampling which might yield $M_{\text{Hyp4}} = 1024$ and $k_{\text{Hyp4}} = 10$.

For the CW fourth-order wavelet, by using $a_{\text{max}1}^{\text{CW4}} \approx 63.5$ and $a_{\text{max}3}^{\text{CW4}} \approx 85.5$ from Eq. (75), and $N_{\text{CW4\_2}} \approx 7$ from Eq. (71), its minimum numbers of input data points, $M_{\text{CW4\_1}}$ and $M_{\text{CW4\_2}}$, are approximately given as

$$M_{\text{CW4\_1}} = 2^k = \frac{63.5 \times (7-1)}{1/3} \geqslant 1143, \quad \text{and} \quad M_{\text{CW4\_2}} = \frac{85.5 \times (7-1)}{1/3} \geqslant 1549, \tag{77}$$

which should be chosen as $M_{\text{CW4}} = M_{\text{CW4\_1}} = M_{\text{CW4\_2}} = 2048$, yielding $k_{\text{CW}} = 11$ for a fast calculation. Thus, in this case, either $a_{\text{max}1}^{\text{CW4}}$ or $a_{\text{max}3}^{\text{CW4}}$ can be employed to estimate M_{CW4}.

A wavelet scale resolution can be estimated independently of its band-peak frequencies, maximum number of scales, minimum number of sampling points N and input data points M. For the CW fourth-order wavelet, its scale resolutions were numerically estimated in Section 6. For the hyperbolic fourth-order wavelet, by using Eq. (41), and $\beta = 0.5$, its scale resolution is the approximate root of the following equation:

$$\lambda \approx \frac{0.0964 \cosh{(4 + 3.14 \omega_d^{\text{Hy4}})}}{(1.274 + \omega_d^{\text{Hy4}})^4}, \tag{78}$$

which yields only one solution of $\omega_d^{\text{Hy4}} \approx 10^{-4}$ for $\lambda = 1$.

To calculate the total number of scales j_{max}, the non-dimensional band-peak frequency at $a = 1$ (for the mother wavelet) must be obtained. For the hyperbolic fourth-order wavelet, by using Eq. (34) with $\beta = 0.5$, we obtain

$$\omega_p^{\text{Hyp4}} = \frac{2 \times 0.5 \times 4}{\pi} \approx 1.274, \tag{79}$$

yielding the wavelet approximate total number of scales j_{max} of 51×10^3. It should be noted that the finer the wavelet scale resolution, the larger its total number of scales j_{max} which establishes a trade-off between them. Thus, depending on the nature of a particular application, a finer scale resolution or a larger total number of scales is chosen. By using Eqs. (51) and (52) with $\sigma = 2$, for the CW fourth-order wavelet, its dimensionless band-peak frequencies are given as

$$\omega_{p1}^{\text{CW4}} \approx 2.8, \tag{80}$$

$$\omega_{p2}^{\text{CW4}} \approx 6.45, \quad \text{and} \quad \omega_{p3}^{\text{CW4}} \approx 6.26. \tag{81}$$

Table 4 summarises numerical parameters of the hyperbolic and CW fourth-order [9] wavelets. For comparison purposes, numerical parameters of the Morlet wavelet with $\omega_\psi = 5.0 \, \text{rad/s}$, hyperbolic and CW second-order wavelets are also given.
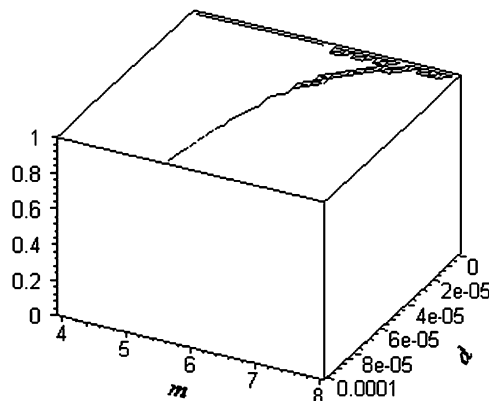

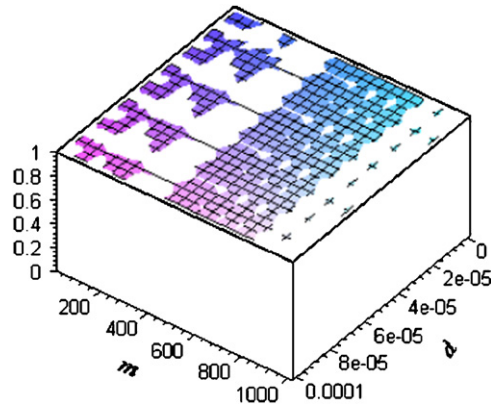Fig. 12. Hyperbolic wavelet scale resolution ("d" on graph) for $6 \leqslant m \leqslant 8$.

Fig. 13. Hyperbolic wavelet scale resolution for $30 \leqslant m \leqslant 10^3$.
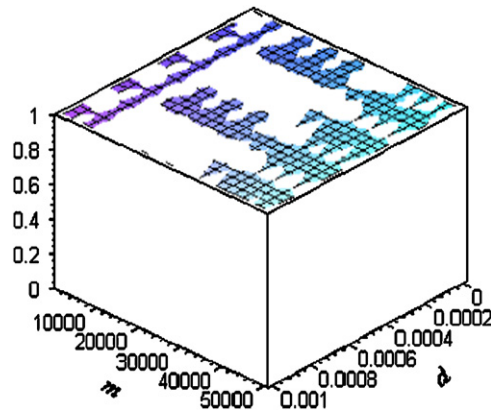

Fig. 14. Hyperbolic wavelet scale resolution for $10^3 \leqslant m \leqslant 5 \times 10^4$.
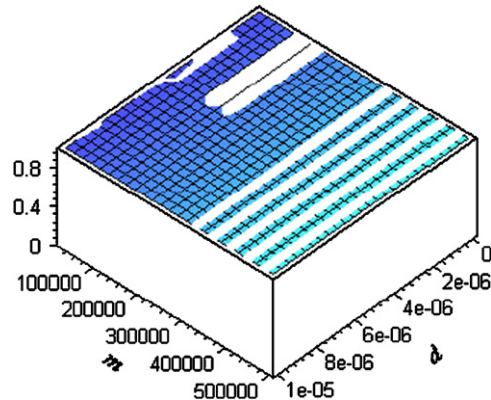

Fig. 15. Hyperbolic scale resolution for $3 \times 10^4 \leqslant m \leqslant 3 \times 10^5$.

As m increases to 6, the hyperbolic wavelet scale resolution becomes finer and approximately approaches 3×10^{-5} as can be seen in Fig. 12. For $8 \leqslant m < 30$, it is undefined. For $10^3 \geqslant m \geqslant 30$, it is graphically displayed in Fig. 13 in which empty regions correspond to prohibited ranges of m. For $10^3 \leqslant m \leqslant 5 \times 10^4$, the scale resolution is graphically plotted in Fig. 14.

As can be seen in Figs. 12–14, for the hyperbolic wavelet family, increasing the wavelet order m does not always yield a finer scale resolution. In fact, for certain values of m, its wavelet scale resolution is undefined or infinite. For $10^4 \leqslant m \leqslant 3 \times 10^4$, from Fig. 14, its wavelet scale resolution is undefined. For $3 \times 10^4 \leqslant m \leqslant 3 \times 10^5$,
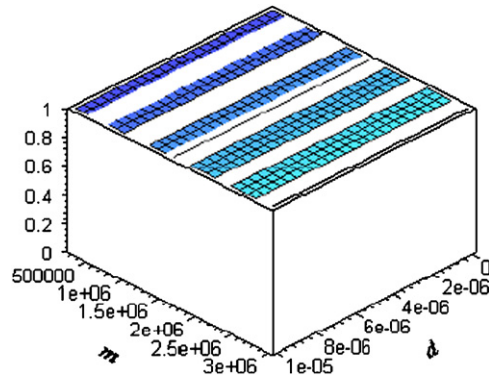
Fig. 16. Hyperbolic scale resolution for $3 \times 10^5 \leqslant m \leqslant 3 \times 10^6$.

Table 4
Approximate parameter values of the Morlet wavelet [9] with $\omega_\psi = 5.0$ rad/s, and second- and fourth-order CW wavelets with $\sigma = 2$ and $\lambda = 0.9$

Wavelet	T	N	$a_{\max}$	M	ω_d	$j_{\max}$
Morlet	3	17	49	4096	0.459	42
Second-order CW	5	13	29	2048	0.3246	14
Second-order hyperbolic	10	9	38	1024	0.2066	11
Fourth-order CW	3	7	85.5	2048	0.15	190[a]
Fourth-order hyperbolic	3	4 or 7	51	512 or 1024	10^{-4}	51×10^3

For the hyperbolic wavelets, $\beta = 0.5$ and $\lambda = 1$.
[a]The largest total number of scales among 82, 190 and 185 estimated by using Eqs. (80) and (81).

it becomes finer as less broken stripes are present as can be seen in Fig. 15. For $m \geqslant 3 \times 10^5$, it becomes finer of approximately $O(10^{-6})$, compared to Fig. 15, as can be seen in Fig. 16, which is a significant improvement over hyperbolic wavelets with lower orders of $m \leqslant 3 \times 10^4$, even though these do possess fine scale resolutions. It should also be noted that there are still empty regions in Fig. 16 which might suggest that these hyperbolic wavelet family members still possess undefined scale resolutions which can be avoided by not choosing the order m in its prohibited ranges, listed as: $300 \leqslant m \leqslant 500$, $800 \leqslant m \leqslant 10^3$, and $10^4 \leqslant m \leqslant 3 \times 10^4$.

One disadvantage of the hyperbolic wavelet is that to obtain a very fine scale resolution, a very large wavelet order m must be used. However, the fourth-order hyperbolic wavelet possesses a fine scale resolution of approximately 10^{-4} and a total number of scales of 51×10^3 (Table 4). For applications of which a finer scale resolution is required, the fourth- and higher-order hyperbolic wavelets can be employed at the expense of having a larger order m and total number of scales. It is also important to stress that the hyperbolic wavelet family scale resolution decreasing rate of $O(10^4)$ is slower than its order m of $O(10^5)$, and more importantly, yielding a slower increasing rate of $O(10^4)$ for its total number of scales $j_{\max}$, which should be small to reduce computational burden. From Table 4, the fourth-order hyperbolic wavelet, even though possesses a larger total number of scales compared to those of the CW wavelets, has a much finer scale resolution which is its prime advantage. Moreover, the second-order hyperbolic wavelet also has a finer scale resolution than that of the CW second-order wavelet as shown in Ref. [9].

7. Experiments

The Duffing oscillator is used in this section as a typical example to show the effectiveness of high-order hyperbolic and Mexican-hat wavelets. The *sym3* wavelet is used as a benchmark for comparison purposes. The Period 2 (as shown in Figs. 17–21) and chaotic states (as shown in Figs. 22–26) of Duffing oscillator are studied using high-order hyperbolic and Mexican-hat wavelet transforms and wavelet power spectra to
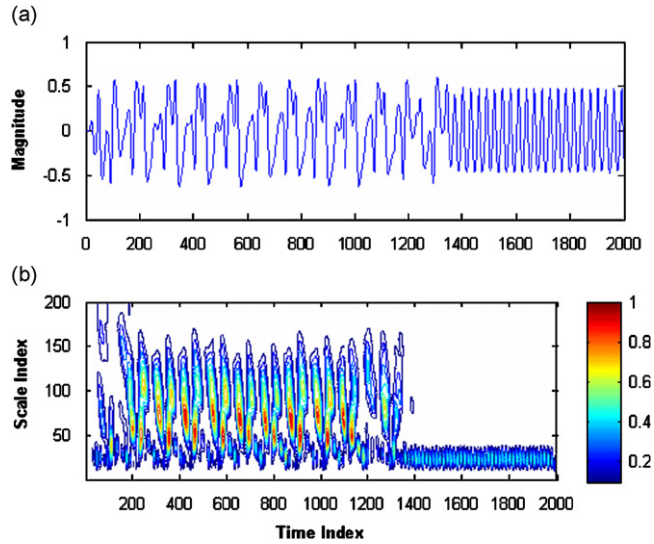
Fig. 17. Magnified time-domain waveform of Duffing Period 2 and a contour plot of its WPS using the *sym3* wavelet.
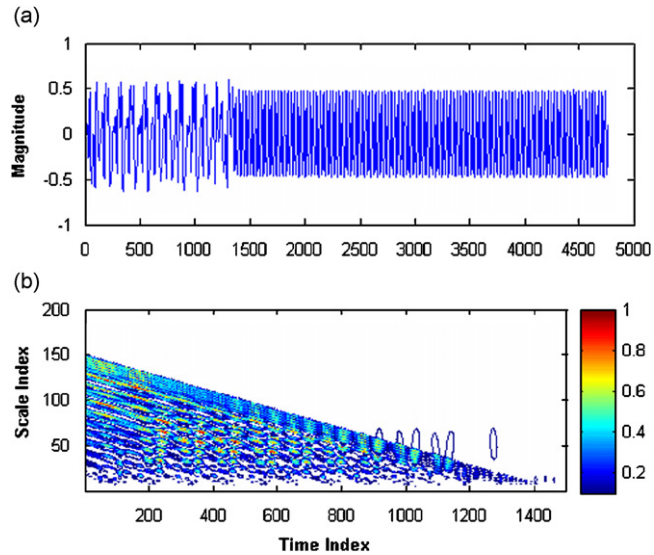

Fig. 18. Time-domain waveform of Duffing Period 2 and contour plot of its hyperbolic WPS using the fourth-order wavelet.

effectively show energy distributions of the input waveform. The wavelet transform (WT) is given in Eq. (2), from that the wavelet power spectrum (WPS) is mathematically given by [13]

$$\mathrm{WPS}(t,\omega) = \mathrm{WT}(t,\omega)\,\mathrm{WT}^*(t,\omega) = \left|\mathrm{WT}(t,\omega)\right|^2. \tag{82}$$

The WT and WPS are used to study signal behaviour because of their ability to effectively show the signals' energy distribution [13], especially for chaotic detection. From Figs. 17–21, it is clear that high-order hyperbolic and Mexican-hat wavelets show consistent results in which the periodicity of the waveform is successfully revealed with the presence of repetitive energy-concentrated contours. It should also be noted that the hyperbolic wavelets yield a larger number of scales (about 250 compared with 90) and a finer resolution than high-order CW wavelets as expected, except the fourth-order hyperbolic wavelet which shows limited information about the input signal. From Fig. 19 subplots (b) and (c), it is clear that the tenth-order
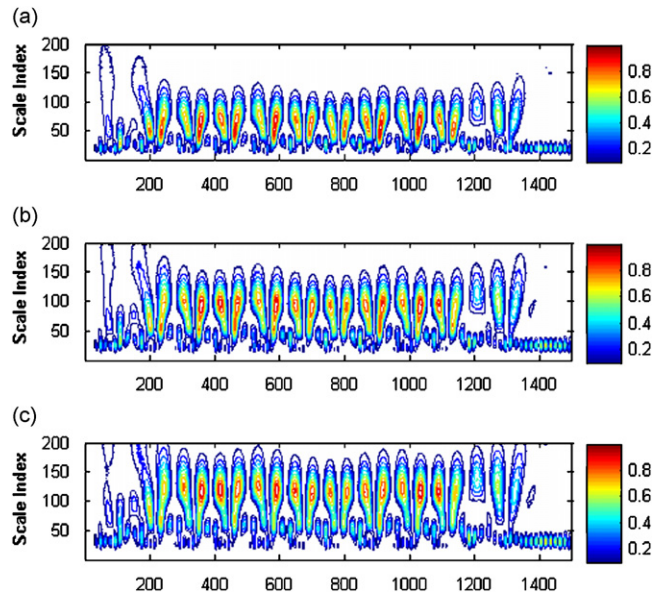
Fig. 19. Contour plots of the hyperbolic WPS of Duffing Period 2 waveform using the sixth- and eighth- and tenth-order wavelets as shown in subplots (a), (b) and (c), respectively.
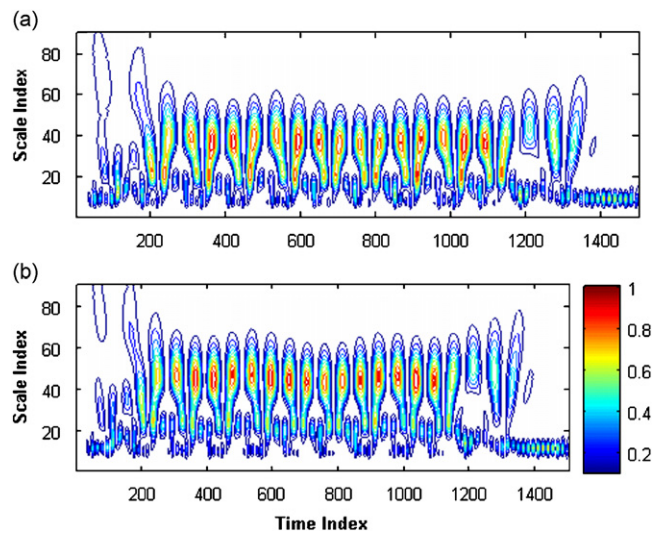

Fig. 20. The CW WPS using the fourth- and sixth-order CW wavelets.

hyperbolic and CW WPS yield a larger total number of scales and an improved scale resolution than the eighth-order WPS, which validates the conclusion made in Section 3. It is also evident that the tenth-order hyperbolic wavelet yields a slight improvement compared with the CW wavelet with a finer scale resolution.

From Figs. 22–26, the hyperbolic and CW high-order wavelets successfully reveal a broad energy distribution of the Duffing chaotic waveform, except the fourth-order hyperbolic wavelet. However, it should be noted that this particular wavelet can still be used to study Duffing oscillator because of its distinct differences between Period 2 and chaotic states as clearly shown in Figs. 18–23. For chaotic detection, the CW wavelets reveal a short "periodic period" in Duffing oscillator which can result in misleading information about the waveform, whereas, the hyperbolic high-order wavelets clearly shows a broad energy distribution with random harmonic peaks which is typical in chaotic waveforms. This suggests that high-order hyperbolic wavelets are more suitable for chaotic detection than CW high-order wavelets.
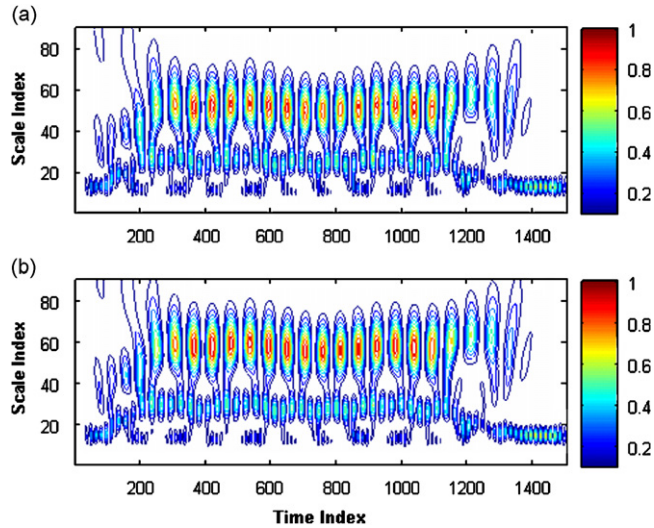
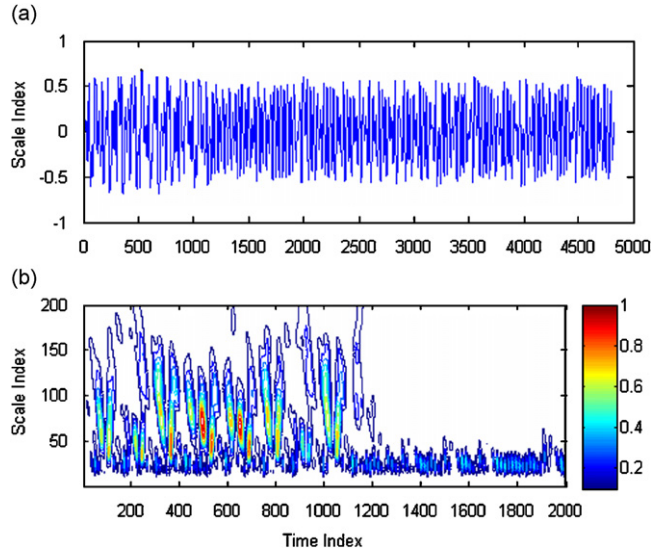Fig. 21. The CW WPS using the eighth- and tenth-order CW wavelets.

Fig. 22. Time-domain of Duffing chaotic waveform and a contour plot of its WPS using the *sym3* wavelet.

8. Conclusions and further work

The meaning of kernel even-order derivative and positive concavity concepts has been discussed in which only even functions were shown to be admissible wavelets. Positive concavity has been employed so that wavelets have positive peaks at the origin and also satisfy kernel admissibility constraints which validate them as admissible kernels for Cohen's time–frequency power spectra. Moreover, for wavelets to be admissible kernels, their parameters β and σ must be numerically set to specific values so that their peaks are unity under DC conditions. For example, the Mexican-hat and hyperbolic second-order wavelets can be considered as admissible kernels only for $\sigma = 2$ and $\beta = 1$, respectively. As a result, it was shown that there exist an infinite number of admissible symmetrical high-order wavelets, yielding an infinite number of kernels for Cohen's time–frequency power spectra.

The negative second-, fourth-, negative sixth-, eighth- and negative tenth-order derivatives of the CW kernel and mth-order derivatives (where m is the even wavelet order) of the first-order hyperbolic kernel have been
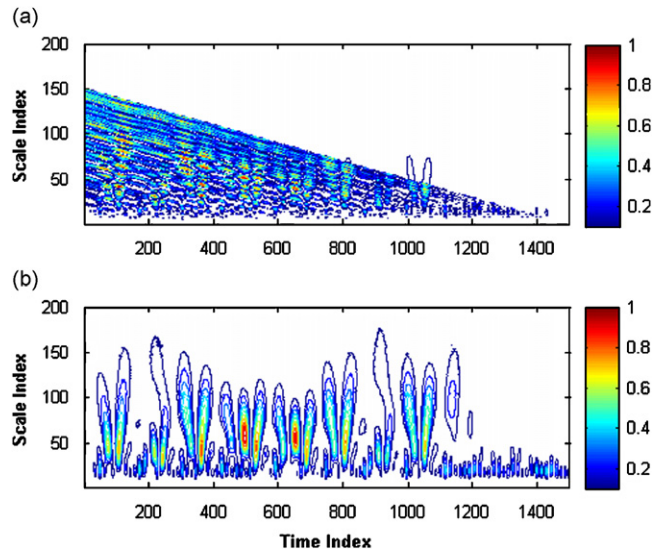
Fig. 23. Contour plots of the hyperbolic WPS of Duffing chaotic waveform using the fourth- and sixth-order wavelets.
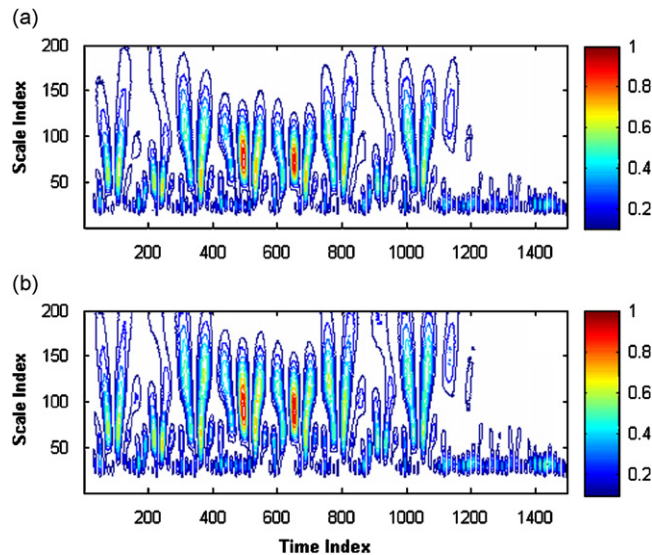

Fig. 24. Contour plots of the hyperbolic WPS of Duffing chaotic waveform using the eighth- and tenth-order wavelets.

explicitly expressed and shown to be admissible wavelets. This allows time–frequency signal processing and wavelet analyses to be correctly linked together which means that new kernels can be found from new wavelets and vice versa, provided that these kernels and wavelets satisfy their admissibility constraints. In the time domain, the hyperbolic and CW wavelet normalisation constants of orders 2–10 have been explicitly expressed and numerically estimated for $\beta = \sigma = 1$. In the frequency domain, the mth-order hyperbolic and fourth-order CW wavelet parameters, including band-peak frequencies, minimum numbers of sampling points, scale limits, scale resolutions and maximum numbers of scales, have been explicitly obtained and numerically estimated for $\beta = 0.5$ and $\sigma = 2$. It was also shown that the higher the wavelet order, the finer its scale resolution, and the larger its total number of scales. Prohibited ranges of the hyperbolic wavelet order m, yielding undefined scale resolutions, have also been identified. Periodic and chaotic detection in the Duffing oscillator has been successfully carried out using high-order hyperbolic and CW wavelets which shows their effectiveness in studying signal behaviour. This is also useful for crack detection in rotors. It has been shown
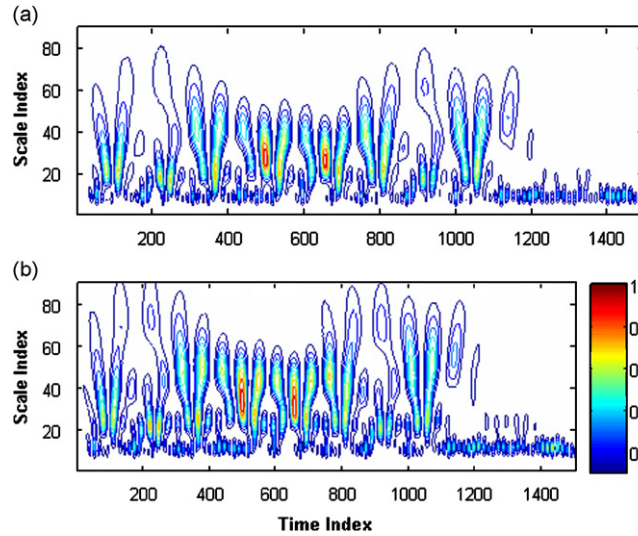
Fig. 25. Contour plots of the CW WPS of Duffing chaotic waveform using the fourth- and sixth-order wavelets.
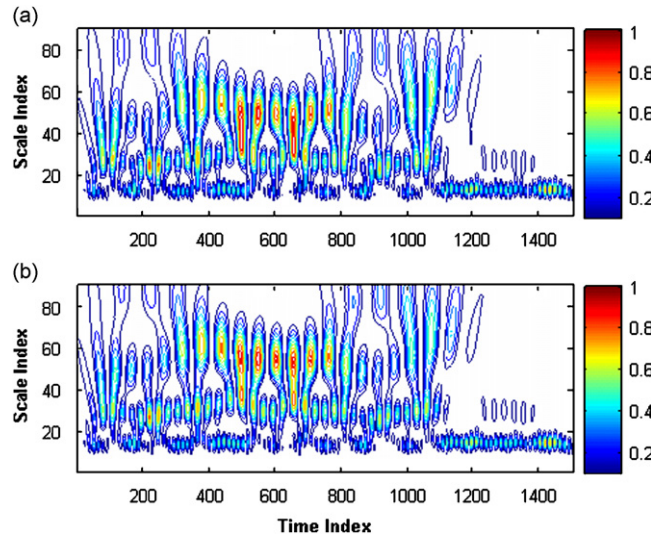

Fig. 26. Contour plots of the CW WPS of Duffing chaotic waveform using the eighth- and tenth-order wavelets.

that the tenth-order hyperbolic and CW wavelets are more effective than the eighth-order wavelets a larger number of scales and a finer scale resolution. More work on using the WT and WPS in crack detection is also in progress.

The CW sixth- to tenth-order wavelets have only been briefly discussed because extensive mathematical manipulations are required to obtain their explicit frequency parameters, which is beyond the scope of this paper. Further work on CW high-order wavelets is worth investigating and will be presented in a future publication. Throughout this paper, it has been shown that high-order hyperbolic and CW wavelets possess finer scale resolutions and are more effective than the second-order hyperbolic and CW wavelets. Higher-order wavelets can also find new applications with further improvements in image processing such as coherent structure detection in turbulence and biomedical signal such as the ECG [12,13], edge detection, image coding [10] and noise reduction [20,21], astrophysics [22–25], plasma physics [26–28], filter banks and wavelet transform calculation efficiency. Some works toward these areas are currently under progress.

References

[1] L. Cohen, *Time–Frequency Analysis*, Prentice-Hall, EngleWoods Cliffs, New York, 1995, pp. 136–289.

[2] L. Cohen, Time–frequency distribution—a review, *IEEE Proceedings* 77 (7) (1989) 941–981.

[3] H.I. Choi, W.J. Williams, Improved time–frequency representation of multi-component signals using exponential kernels, *IEEE Transactions on Signal Processing* 37 (6) (1989) 862–871.

[4] A.H. Costa, G.F. Boudreaux-Bartels, Design of time–frequency representation using a multiform, tiltable exponential kernel, *IEEE Transactions on Signal Processing* 43 (10) (1995) 2283–2301.

[5] K.N. Le, K.P. Dabke, G.K. Egan, Hyperbolic kernel for time–frequency power spectrum, *Optical Engineering* 42 (8) (2003) 2400–2415.

[6] T.A.C.M. Claasen, W.F.G. Mecklenbrauker, The Wigner distribution—a tool of time–frequency signal analysis. Part I: Discrete-time signals, *Philips Journal of Research* 35 (3) (1980) 217–250.

[7] T.A.C.M. Claasen, W.F.G. Mecklenbrauker, The Wigner distribution—a tool for time–frequency signal analysis. Part III: Relations with other time–frequency signal transformations,, *Philips Journal of Research* 35 (6) (1980) 372–389.

[8] T.A.C.M. Claasen, W.F.G. Mecklenbrauker, The Wigner distribution—a tool for time–frequency signal analysis. Part II: Continuous-time signals, *Philips Journal of Research* 35 (4–5) (1980) 276–300.

[9] K.N. Le, K.P. Dabke, G.K. Egan, The hyperbolic wavelet function, *SPIE Aerosense Proceedings: Wavelet Applications VIII*, Orlando, FL, USA, SPIE, April 2001.

[10] R.C. Gonzalez, R.E. Woods, *Digital Image Processing*, second ed., Prentice-Hall, Upper Saddle River, New Jersey, 2002, pp. 567–600.

[11] D. Marr, *Vision: A Computational Investigation into the Human Representation and Processing of Visual Information*, W.H. Freeman and Company, San Francisco, 1982, pp. 54–67.

[12] P.S. Addison, J.N. Watson, T. Feng, Low-oscillation complex wavelets, *Journal of Sound and Vibration* 254 (4) (2002) 733–762.

[13] K.N. Le, K.P. Dabke, G.K. Egan, Hyperbolic wavelet power spectra of non-stationary signals, *Optical Engineering* 42 (10) (2003) 3017–3037.

[14] D. Jordan, R.W. Miksad, E.J. Powers, Implementation of the continuous wavelet transform for digital time series analysis, *Review of Scientific Instruments* 68 (3) (1997) 1484–1494.

[15] I. Daubechies, *Ten Lectures on Wavelets*, SIAM, Philadelphia, 1992, pp. 20–100.

[16] C.S. Burrus, R.A. Gopinath, H. Guo, *Introduction to Wavelets and Wavelet Transform: A Primer*, Prentice-Hall, Upper Saddle River, New Jersey, 1998, pp. 1–100.

[17] E. Kreyszig, *Advanced Engineering Mathematics*, sixth ed., John Wiley & Sons, New York, 1988, pp. 596–598.

[18] H. Zhang, et al., Optical implementation of a photorefractive joint transform correlator with wavelet, *Optics Communications* 181 (4–6) (2000) 223–230.

[19] K.N. Le, K.P. Dabke, G.K. Egan, Signal detection using non-unity kernel time–frequency distributions, *Optical Engineering* 40 (12) (2001) 2866–2877.

[20] S. Sardy, P. Tseng, A. Bruce, Robust wavelet denoising, *IEEE Transactions on Signal Processing* 49 (6) (2001) 1146–1152.

[21] C.-W. Tang, H.-M. Hang, A feature-based robust digital image watermarking scheme, *IEEE Transactions on Signal Processing* 51 (4) (2003) 950–959.

[22] P. Vielva, et al., Combining maximum-entropy and the Mexican-hat wavelet to reconstruct the microwave sky, *Monthly Notices of the Royal Astronomical Society* 328 (1) (2001) 1–16.

[23] P. Vielva, et al., Predicted Plank extragalactic point-source catalogue, *Monthly Notices of the Royal Astronomical Society* 326 (1) (2001) 181–191.

[24] J.L. Sanz, et al., Wavelets applied to cosmic microwave background maps: a multiresolution analysis for denoising, *Monthly Notices of the Royal Astronomical Society* 309 (3) (1999) 672–680.

[25] E. Martinez-Gonzalez, et al., The performance of spherical wavelets to detect non-Gaussianity in the cosmic microwave background sky, *Monthly Notices of the Royal Astronomical Society* 336 (1) (2002) 22–32.

[26] Z. Popovic, S. Satpathy, Cooperative Jahn–Teller coupling in the manganites, *Physical Review Letters* 84 (7) (2000) 1603–1606.

[27] D. Roberts, A.R. Liddle, D.H. Lyth, False vacuum inflation with a quartic potential, *Physical Review D* 51 (8) (1995) 4122–4128.

[28] T. Yildirim, A.B. Harris, Quantum dynamics of a hydrogen molecule confined in a cylindrical potential, *Physical Review B* 67 (24) (2003) 245413/1–15.